UNIVERSIDAD DE CHILE
FACULTAD DE CIENCIAS FÍSICAS Y MATEMÁTICAS
DEPARTAMENTO DE INGENIERÍA ELÉCTRICA

DEVELOPMENT OF A SINGLE-ENDED LNA & TECHNICAL-ECONOMIC COMPARISON WITH A DIFFERENTIAL IMPLEMENTATION FOR THE CHARTS PROJECT

MEMORIA PARA OPTAR AL TÍTULO DE
INGENIERO CIVIL ELÉCTRICO

FRANCISCO TADEO MUÑOZ PAVICICH

PROFESOR GUÍA:
TOMÁS CASSANELLI ESPEJO

MIEMBROS DE LA COMISIÓN:
RICARDO FINGER CAMUS
TOMÁS CASSANELLI ESPEJO
JUAN MENA PARRA

Este trabajo ha sido parcialmente financiado por el programa Dunlap Seed Funding y el fondo ANID QUIMAL. T.C. y F.C. agradecen el apoyo de ANID BASAL FB210003 y fondo de astronomía: ANID / Fondo 2023 QUIMAL / QUIMAL230001. El Instituto Dunlap es financiado mediante una donación establecida por la familia David Dunlap y University of Toronto.

SANTIAGO DE CHILE
2025

Resumen

Las ráfagas rápidas de radio o *FRB* por sus siglas en inglés, son fenómenos astrofísicos que han capturado la atención de la comunidad científica desde su descubrimiento en 2007. Estas ráfagas son emisiones de radio extremadamente breves (milisegundos) y potentes, que se originan fuera de nuestra Galaxia y se caracterizan por su naturaleza efímera.

El estudio de este fenómeno promete realizar un aporte significativo a la comprensión del universo, incluyendo aspectos como la naturaleza de la materia oscura, la evolución de las galaxias y otros temas astrofísicos relevantes. Sin embargo, la detección de estos fenómenos es un desafío debido a su corta duración y a la gran cantidad de ruido presente en el espacio.

En este contexto, se desarrolla el proyecto CHARTS (*Canadian-Chilean Array for Radio Transit Studies*), un esfuerzo conjunto entre la Universidad de Chile y la University of Torornto que busca desarrollar un radiotelescopio capaz de detectar y ubicar estos fenómenos.

Este trabajo se centra en el desarrollo de un amplificador de bajo ruido (LNA), diseñado para operar en la banda de frecuencias de CHARTS (300–500 MHz) y una comparación técnico-económica con la implementación de un amplificador diferencial.

Se describe en profundidad el proceso de diseño y la implementación del LNA, incluyendo la selección de componentes, el diseño de circuitos y la simulación de rendimiento. También se presentan los resultados de las pruebas realizadas para evaluar el rendimiento del LNA, incluyendo la ganancia, la temperatura de ruido y las impedancias de entrada y salida.

A continuación, se realiza un análisis técnico-económico que compara la implementación de un LNA diferencial con la implementación *single-ended* propuesta en este trabajo. En este se consideran factores como el costo de los componentes, la complejidad del diseño y la facilidad de implementación.

Finalmente, se discuten las implicaciones de los resultados obtenidos y se presentan conclusiones sobre la viabilidad de la implementación del LNA single-ended en el contexto del proyecto CHARTS. Este trabajo contribuye al avance del conocimiento en el campo de la astrofísica y la ingeniería eléctrica, proporcionando una base para futuras investigaciones y desarrollos en la instrumentación radioastronómica.

Abstract

Fast radio bursts, or FRBs, are astrophysical phenomena that have captured the attention of the scientific community since their discovery in 2007. These bursts are extremely brief (milliseconds) and powerful radio emissions that originate outside our Galaxy and are characterized by their transient nature.

The study of these phenomena promises to make a significant contribution to understanding the universe, including aspects such as the nature of dark matter, galaxy evolution, and other relevant astrophysical topics. However, detecting these bursts is challenging due to their short duration and the large amount of noise present in space.

In this context, the CHARTS project, (Canadian-Chilean Array for Radio Transit Studies) was established, a joint effort between the Universidad de Chile and the University of Toronto which seeks to develop a radio telescope capable of detecting and locating these phenomena.

This work focuses on the development of a low-noise amplifier (LNA), designed to operate in the CHARTS frequency band (300–500 MHz), and a technical-economic comparison with the implementation of a differential amplifier.

The design process and implementation of the LNA are described in detail, including component selection, circuit design, and performance simulation. The results of testing conducted to evaluate the LNA's performance are also presented, including gain, noise temperature, and input and output impedance.

Subsequently, a technical-economic analysis is conducted that compares the implementation of a differential LNA with the single-ended implementation proposed in this work. This analysis considers factors such as component cost, design complexity, and the ease of implementation.

Finally, the implications of the obtained results are discussed and conclusions are presented regarding the viability of implementing the single-ended LNA in the context of the CHARTS project. This work contributes to advancing knowledge in the field of astrophysics and electrical engineering, providing a foundation for future research and developments in radio astronomical instrumentation.

A mis padres Isabel y Álvaro.

Acknowledgments

First and foremost, I would like to express my deepest gratitude to my family. To my grandparents, Alejandra, Jorge, Lucy, and Rubén, for their unconditional love; to my parents, for their unwavering support despite the distance; and to my brother, for always being by my side, offering guidance and encouragement throughout these final years of my studies.

To my partner María José and lifelong friends Mateo, Valentina, Javiera, Anais, Sebastián, and Osvaldo, with whom I have grown and shared invaluable experiences—I will always be grateful for your companionship and support.

To my faculty friends, Francisca Godoy, Meloddy Guzmán, Bárbara Aguayo, Roberto Zuñiga, Tomás Vatel, Benjamín Llancao, Diego Vega, Raimundo Varleta, and Gabriel Raquiman, your friendship has been essential in this journey, and I am certain that without you, I would not be the same person.

To my thesis advisor, Tomás Cassanelli, for granting me this incredible opportunity and for his constant support and guidance whenever I needed it. To my colleagues and friends in the CHARTS project—Gonzalo Burgos and Sebastián Manosalva—with whom I have grown both professionally and personally. I also extend my gratitude to our colleagues at the Millimeter Wave Laboratory, especially Claudia San Martin, Juan Riquelme, José Pizarro, Álvaro Morales, Diego Gallardo, Max Prieto and José Vargas, for all the laugths and taca-taca matches.

Finally, I wish to express my heartfelt appreciation to the Faculty of Physical and Mathematical Sciences at the Universidad de Chile for being my academic home during these years. A special thanks to the Department of Electrical Engineering and to Karina Ávila, head of the Electronics Laboratory, for always welcoming us and providing a space to test our ideas.

To all of you, I owe my education and personal growth. I extend my deepest gratitude.

Table of Content

List of Tables

List of Figures

Chapter 1

Introduction

1.1 Fast Radio Bursts

Fast radio burst (FRB) are intense, microsecond/millisecond-duration (∼1–100 µs) pulses of coherent radio emission detected across a wide frequency range, from 110 MHz to 8 GHz (Pleunis et al. 2021; Gajjar et al. 2018; Bethapudi et al. 2023). These enigmatic signals originate from extragalactic sources, with their underlying astrophysical mechanisms not fully understood (Petroff et al. 2022; Zhang 2023). Since their initial discovery in 2007 (Lorimer et al. 2007), FRB have been distinguished by their frequency-dependent dispersion, a signature that confirms their cosmological distances.

By 2021, the Canadian Hydrogen Intensity Mapping Experiment (CHIME) and its FRB backend had documented over 600 FRBs (CHIME/FRB Collaboration et al. 2021), including "repeaters" exhibiting periodic behavior. Radio observatories have identified two distinct types: repeating sources (∼4–10 % of total events) and one-off bursts. Localized repeaters have enabled multi-wavelength studies (Marcote et al. 2020; Nimmo et al. 2022), yielding insights into their periodicity (Braga et al. 2025), energy distributions (Cruces et al. 2021), and polarimetric properties (Mckinven et al. 2023).

One-off events, though more numerous (Shannon et al. 2025), present localization challenges. Two main approaches exist: Very Long Baseline Interferometry (VLBI) techniques for simultaneous multi-location detection (Cassanelli et al. 2024; Leung et al. 2024; Cassanelli et al. 2022) or statistical analysis of bright nearby events (Bhardwaj et al. 2024).

The significance of FRB research extends beyond their recent discovery, as these phenomena represent powerful tools for probing the intergalactic medium (IGM) and addressing fundamental cosmological questions (Macquart et al. 2020). Researchers have successfully identified host galaxies for several FRBs and linked some events to Galactic magnetars (CHIME/FRB Collaboration et al. 2021), providing crucial clues about their origins. This scientific potential has catalyzed the development of dedicated observational infrastructure, including specialized facilities such as CHIME/FRB (CHIME/FRB Collaboration et al. 2021), Bustling Universe Radio Survey Telescope in Taiwan (BURSTT; Lin et al. 2022)

, and Galactic Radio Explorer (GRex; Shila et al. 2025; Connor et al. 2021), each designed to capture different aspects of these enigmatic cosmic signals.

1.2 Canadian-Chilean Array for Radio Transient Studies (CHARTS)

The Canadian-Chilean Array for Radio Transient Studies (CHARTS) project is a collaboration between University of Toronto (UofT) and Universidad de Chile to build a radio interferometer experiment. This project is designed to detect and study FRB, focusing on low-frequencies observations in the 300–500 MHz range.

The CHARTS system will consist of an array of 256 elements designed to observe the 300–500 MHz frequency range. The signals captured by the antennas will pass through an low-noise amplifier (LNA), which is a crucial component in the analog signal reception process. The primary role of the LNA is to amplify weak signals while minimizing the introduction of additional noise into the reception chain.

For optimal performance, the CHARTS' LNA must provide a minimum gain of 50 dB while maintaining a system noise temperature below 100 K. This design maximizes the system's sensitivity, enhancing the detection capability for radio transient phenomena such as FRB. The effective functioning of this initial amplification stage is vital for achieving efficient signal processing with minimal distortion.

After amplification, the signals pass through a frequency division multiplexer (FDM), where the outputs from 8 antennas are multiplexed into a single analog-to-digital converter (ADC) channel. These digitized signals are then sent to radio frequency system-on-chips (RFSoCs), which are field programmable gate arrays (FPGAs) equipped with high-speed ADCs. Once digitized, the back-end processing begins. This stage corresponds to the array correlator, which computes the power spectral density from the radio data and performs beamforming on the sky (F-engine and X-engine). The complete processing chain, from signal reception to back-end processing, is illustrated in fig. 1.1.

The LNA design, along with other designs developed in this project such as specialized FDM and antenna design, represents a significant advancement in radio astronomy engineering (Cassanelli et al. 2025). With this development, CHARTS can detect and study low-frequency radio signals, enabling radio transient observations from the Southern Hemisphere.

CHARTS will be implemented at Laguna Carén, located in the Santiago Metropolitan Region of Chile. The array will be gradually deployed, with the first stage involving the installation of 32 antennas, followed by subsequent expansions to reach the full 256-element array.

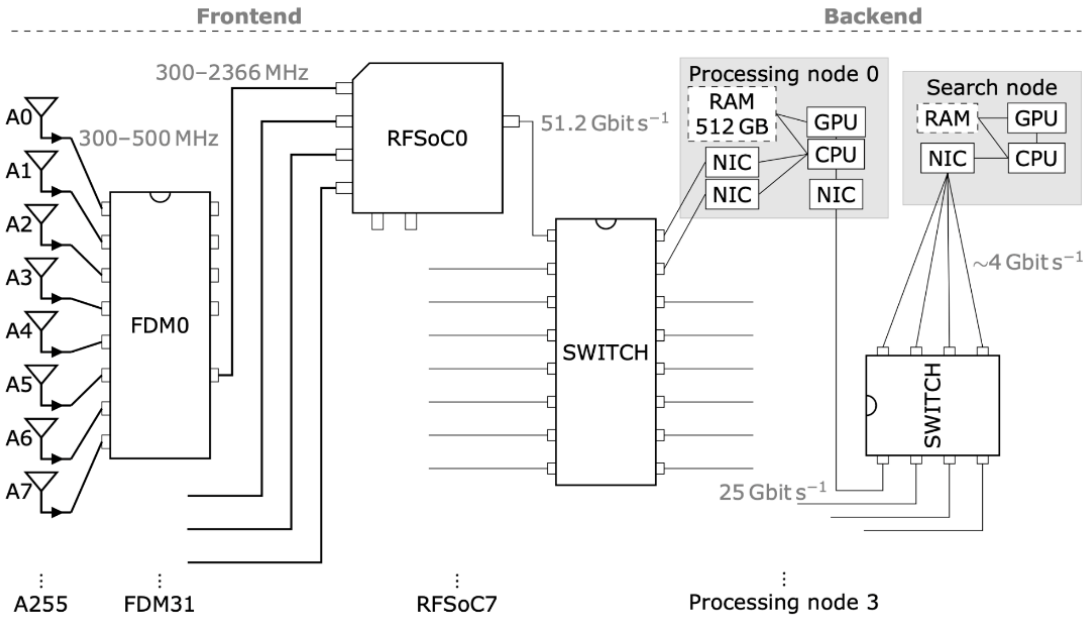

Figure 1.1: CHARTS system architecture showing the signal processing flow from antennas to final analysis. The Frontend contains antenna arrays (A0-A255) that capture 300-500 MHz signals, which are combined by FDM and digitized by RFSoC units. The Backend uses network switches to distribute the digitized data to multiple processing nodes equipped with graphics procesing unit (GPU), central processing unit (CPU), random access memory (RAM) , and network interface card (NIC). A dedicated search node performs final pattern detection and analysis.

1.2.1 CHARTS-8 and CHARTS Path Finder Telescope (CPT)

To validate the various stages of the CHARTS reception chain, antennas, LNA, FDM, and RFSoC programming, comprehensive testing was conducted for the complete analog chain.

To facilitate these tests, a subset of the full CHARTS array was deployed in Cerro Calán at Universidad de Chile's Astronomy Department (DAS) by the AstroLab team. AstroLab is a multidisciplinary group of astronomers, physicists, and electrical engineers dedicated to understanding astronomical events across the long-wavelength radio regime and optical wavelengths. Our scientific interests include pulsars, millisecond pulsars, and fast transients such as FRBs, with a particular focus on designing and building specialized instruments for high-cadence transient observations. The team's expertise spans radio instrumentation (analog and digital component development), big data analysis, and scientific interpretation of observational results. AstroLab actively works with data and instruments from major telescopes, including APEX, ALMA, Effelsberg and CHIME. This testbed enabled practical evaluation of the developed components and system integration.

CHARTS-8 is a scaled-down implementation of CHARTS, consisting of eight antennas connected to the FDM and subsequently to the RFSoC-based backend. This setup allowed for integrated testing of the analog and digital subsystems in a realistic operational environment. With the CHARTS-8 array, the team could assess the performance of the reception chain,

including the LNA, FDM, and RFSoC, under conditions that closely mimic those expected in the full CHARTS deployment. Studies related to radio frequency interference (RFI), the noise temperature of the chain, and overall system performance were conducted, providing valuable insights into the system's capabilities and limitations.

The CHARTS Path Finder Telescope (CPT) is a 3-meter single-dish radio telescope constructed by AstroLab in collaboration with the Millimeter Wave Lab Laboratory (MWL), specifically optimized for observations in the megahertz frequency range. The CPT served as a prototype and technology demonstrator for the larger CHARTS project, enabling early validation of critical subsystems and methodologies, and eventually will be used to perform VLBI together with CHARTS and a twin radio telescope being developed in Temuco, Chile, at Universidad de la Frontera (UFRO).

Both the CHARTS-8 array and the CPT use the single-ended LNA for their initial tests. The most significant outcomes from these campaigns include detailed RFI measurements and successful end-to-end verification of the entire reception chain, demonstrating the system's readiness for further scaling and deployment.

1.3 Objectives

The primary objective of this work is to design and implement an LNA to serve as the first amplification stage for the CHARTS project. This LNA will be evaluated and compared with a differential implementation developed by Dr. Albert Wai Kit Lau at the UofT, to identify the most effective solution for the project's requirements.

The work begins with a comprehensive definition of the technical requirements for the amplification stage, establishing the essential characteristics and performance criteria that the LNA must fulfill. This step ensures that the design process is guided by clear objectives tailored to the specific needs of the project.

Subsequently, the process involves the selection of a suitable integrated circuit (IC) amplifier, followed by the detailed design, simulation, and implementation of the LNA. Rigorous performance testing was conducted to characterize and validate key parameters such as noise temperature, gain, and input reflections.

Finally, the results obtained from the single-ended LNA were compared with those of the differential LNA developed by Dr. Lau at the UofT. This comparison encompassed key technical specifications—such as receiver noise temperature and gain—as well as an economic analysis focused on the costs of principal components and cabling required for each implementation.

Through this comparative analysis, the work aims to provide a recommendation regarding the most suitable amplification solution for the CHARTS project, balancing both technical performance and cost-effectiveness.

It is important to note that the scope of this work is focused on the LNA and its implementation, and does not encompass the design and construction of the single-ended antenna,

Figure 1.2: (a) The antenna is receiving noise from various directions, represented by the coordinates (θ, ϕ), resulting in an established antenna temperature denoted as T_A. (b) This illustrates the equivalent model. Figures adapted from Stutzman & Thiele 2012, Ch. 4, p. 104.

the LNA's enclosure, or other related radio frequency (RF) hardware components developed in the context of this work.

1.4 Background

The following sections provide a review of the theoretical framework relevant to this project and discuss similar projects conducted in recent years that have served as a guide for this report.

1.4.1 Theoretical Framework

Designing an LNA for radio astronomy applications requires a thorough understanding of key concepts in RF circuits and radio astronomy. This section will outline the essential theoretical principles that will serve as the foundation for developing the proposed amplifier for the CHARTS project.

Antenna Noise

Antenna temperature is a critical parameter for accurately determining system noise performance, gain requirements, and overall signal-to-noise ratio characteristics.

The antenna captures incident noise through its radiation pattern. Due to the incoherent nature of noise sources, noise power contributions are statistically additive, resulting in a cumulative noise contribution to the system output. As illustrated in fig. 1.2, the antenna's radiation resistance can be equivalently modeled as a noise source characterized by an effective noise temperature (T_A).

T_A refers to the equivalent noise temperature, which represents the noise generation mechanism of a system. This equivalent temperature generates the same noise power, denoted as P_N, as the antenna would produce in its operating environment.

The noise temperature model serves as a fundamental tool for quantifying the noise power generated by antennas, estimating the system's noise figure, and predicting the signal-to-noise ratio (SNR). Based on noise theory, we can derive the Nyquist noise equation:

$$P_N = kT\Delta f \tag{1.1}$$

Where:

- P_N = Available noise power [W]
- k = Boltzmann's constant = 1.38×10^{-23} J/K
- T = Noise temperature [K]
- Δf = Receiver bandwidth [Hz]

This phenomenon, referred to as Nyquist noise or Johnson noise, is the thermal noise produced in a resistive system. The noise power at the antenna output, denoted as P_N, can be determined using the antenna's noise temperature T_A.

The total system noise power is the sum of the antenna output noise and the input receiver noise power. Similarly, the total system noise temperature can be calculated as follows:

$$T_{\text{sys}} = T_A + T_r \tag{1.2}$$

where T_r denotes the receiver noise added to the signal, expressed in terms of temperature, illustrating how noise temperatures are additive within the system.

Noise Temperature

Noise is a critical factor that limits the performance of reception systems across various domains, from radio telecommunications to astronomical observations.

Two key metrics for quantifying this noise are the noise figure (NF) and the noise temperature, each offering a unique perspective on the system's noise characteristics.

The NF and the noise temperature are fundamentally two different representations of the same underlying phenomenon: SNR degradation in a system. Although they approach noise characterization from different angles, they are mathematically interconvertible and provide complementary insights into system performance.

The noise factor (F) is used primarily in general engineering applications and is defined as the ratio of input SNR to output SNR. Mathematically, F is expressed as (Pozar 2011):

$$F = \frac{\text{SNR}_{\text{in}}}{\text{SNR}_{\text{out}}} \tag{1.3}$$

then the NF in decibels is calculated as:

$$NF\,(\mathrm{dB}) = 10\log_{10}(F) \tag{1.4}$$

and for cascaded systems, the total F is calculated using Friis' formula (Pozar 2011):

$$F = F_1 + \frac{F_2 - 1}{G_1} + \frac{F_3 - 1}{G_1 G_2} + \cdots + \frac{F_N - 1}{\prod_{n=1}^{N-1} G_n} \tag{1.5}$$

The noise temperature, commonly used in radio astronomy and specialized systems such as radio telescopes, provides an equivalent temperature representation of the system noise. The relationship between F and noise temperature (T_e) is given by:

$$T_e = T_0(F - 1) \tag{1.6}$$

where T_0 is the standard reference temperature, typically 290 K. This equation allows conversion between the F (a dimensionless ratio) and the equivalent noise temperature (in Kelvin), facilitating direct comparison of system noise performance in different representations.

For cascaded systems, the receiver noise temperature follows a similar Friis-like formula (Pozar 2011):

$$T_{\mathrm{R}} = T_{\mathrm{R1}} + \frac{T_{\mathrm{R2}}}{G_1} + \frac{T_{\mathrm{R3}}}{G_1 G_2} + \cdots + \frac{T_{\mathrm{Rn}}}{G_1 G_2 \cdots G_{n-1}} \tag{1.7}$$

Achieving a low noise temperature is essential for maximizing the sensitivity and scientific output of the CHARTS interferometer. A lower system noise temperature directly improves the minimum detectable flux density, enabling the detection of fainter transient events such as FRBs within the targeted frequency band.

System sensitivity and detection rates depend on the combined noise contributions from the antenna and receiver, see eq. (1.2). As the first element in the receiver chain, the LNA has the greatest impact on overall noise performance, as described by eq. (1.7). Therefore, minimizing the LNA's noise temperature is critical for achieving optimal performance in the CHARTS array.

Noise Figure of a Mismatched Amplifier:

In practical RF systems, impedance mismatches between the source and the amplifier input can degrade the noise performance. The noise figure of a mismatched amplifier is higher than that of a perfectly matched one, and its value depends on the source reflection coefficient (Γ_S or S_{11}) and the amplifier's noise parameters.

The noise figure for a mismatched amplifier (F_m) is given by (Pozar 2011):

$$F_m = 1 + \frac{F - 1}{1 - |\Gamma|^2} \tag{1.8}$$

where:

- F is the minimum noise factor of the amplifier,

- Γ is the source reflection coefficient,

This equation shows that the noise figure increases as the source impedance deviates from the optimum value. Therefore, careful impedance matching is essential to achieve the lowest possible noise figure in LNA design.

Excess Noise Ratio (ENR):

A key parameter in practical noise measurements is the excess noise ratio (ENR), which quantifies the noise output of a specialized noise source relative to thermal noise at the standard temperature T_0. ENR is defined as (Pozar 2011):

$$ENR = \frac{T_{hot} - T_0}{T_0} \tag{1.9}$$

where T_{hot} is the effective noise temperature of the noise source when it is "on." ENR is typically expressed in decibels:

$$ENR\,(\text{dB}) = 10 \log_{10} \left(\frac{T_{hot} - T_0}{T_0} \right) \tag{1.10}$$

Specialized noise generators with known ENR values are widely used to characterize the noise performance of active components such as amplifiers and receivers. By connecting a noise source with a calibrated ENR to the input of the Device Under Test (DUT) and measuring the output noise power, one can accurately determine the noise figure or noise temperature of the device using methods such as the Y-factor (Pozar 2011, Ch. 10.1, pp. 501–502).

Both metrics can be measured using sophisticated techniques. The Y-factor method, also called the hot-cold test, is particularly notable and involves:

1. Connecting a system to two loads at different known temperatures (or using a noise source with known ENR).
2. Measuring output noise power.
3. Calculating the equivalent noise temperature or noise figure.

By understanding the noise figure, noise temperature, and the use of ENR in measurement setups, engineers and scientists can better characterize and enhance the performance of complex reception systems in different fields.

Scattering Parameters

Scattering parameters (S-parameters) are essential for analyzing the behavior of networks and devices that operate at radio frequencies. They describe the relationship between incident and reflected voltage waves at the network's ports.

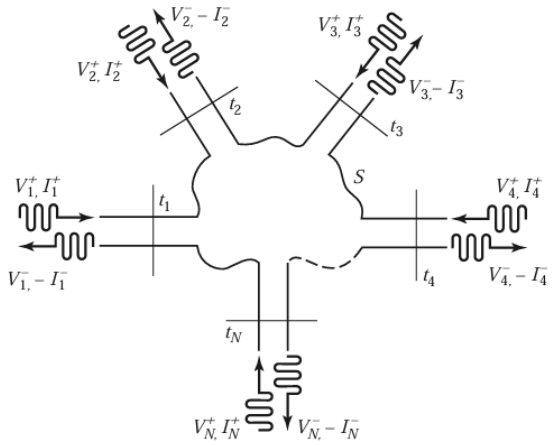

Figure 1.3: N-port variable definitions for S-parameters. Figure adapted from Pozar 2011, Ch. 4.2, p. 174.

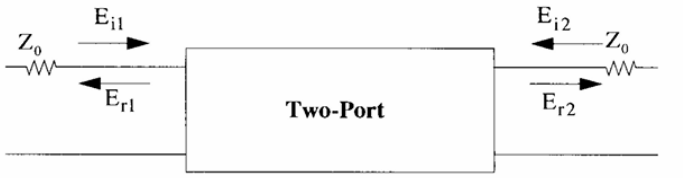

Figure 1.4: Two port variable definitions for S-parameters. Extracted from Lee 2004.

The general matrix representation of S-parameters for an N-port network is given by:

$$\begin{bmatrix} V_1^- \\ V_2^- \\ \vdots \\ V_N^- \end{bmatrix} = \begin{bmatrix} S_{11} & S_{12} & \cdots & S_{1N} \\ S_{21} & S_{22} & \cdots & S_{2N} \\ \vdots & \vdots & \ddots & \vdots \\ S_{N1} & S_{N2} & \cdots & S_{NN} \end{bmatrix} \begin{bmatrix} V_1^+ \\ V_2^+ \\ \vdots \\ V_N^+ \end{bmatrix} \tag{1.11}$$

For a two-port network, from fig. 1.4, normalized wave variables are defined as:

$$a_1 = E_{i1}/\sqrt{Z_0} \tag{1.12}$$

$$a_2 = E_{i2}/\sqrt{Z_0} \tag{1.13}$$

$$b_1 = E_{r1}/\sqrt{Z_0} \tag{1.14}$$

$$b_2 = E_{r2}/\sqrt{Z_0} \tag{1.15}$$

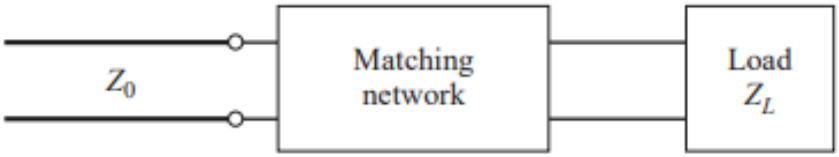

Figure 1.5: General impedance matching network schematic

and so on, the individual S-parameters can be expressed as:

$$s_{11} = \frac{b_1}{a_1} = \frac{E_{r1}}{E_{i1}} = \Gamma_1 \tag{1.16}$$

$$s_{21} = \frac{b_2}{a_1} = \frac{E_{r2}}{E_{i1}} \tag{1.17}$$

$$s_{22} = \frac{b_2}{a_2} = \frac{E_{r2}}{E_{i2}} = \Gamma_2 \tag{1.18}$$

$$s_{12} = \frac{b_1}{a_2} = \frac{E_{r1}}{E_{i2}} \tag{1.19}$$

In RF circuit analysis, S-parameters characterize circuit behavior: S_{11} and S_{22} represent input and output reflection coefficients, indicating how much signal is reflected at each port; S_{21} measures forward transfer gain, showing signal transmission (amplification or attenuation) through the circuit; S_{12} quantifies reverse transfer gain, representing signal transmission in the opposite direction.

S-parameters are fundamental in RF and microwave engineering, providing a comprehensive quantitative description of network behavior across high-frequency applications. Their versatility enables precise analysis and optimization of complex electronic systems.

Impedance Matching in RF Circuits

Impedance matching is a critical design consideration in RF circuits, crucial for maximizing power transfer and minimizing unwanted reflections. The maximum power transfer theorem states that maximum power is transferred from a source to a load when the load impedance is equal to the complex conjugate of the source impedance (Lee 2004; Pozar 2011).

The primary objective of impedance matching is to transform the load impedance Z_L to the system's characteristic impedance Z_0, typically $50\,\Omega$.

Impedance mismatches result in signal reflections, which can be quantified through three key parameters: the reflection coefficient, Γ, which is equivalent to the S_{11} parameter, return loss ratio (RL), and standing wave ratio (SWR). These metrics provide critical insights into the quality of impedance matching in RF systems, with lower RL values and SWR closer to 1 indicating better impedance matching and reduced signal reflections.

Characteristic impedance selection involves a trade-off between minimizing losses and maximizing power handling capacity. When the load is complex ($Z_L = R_L + jX_L$), especially when $R_L < Z_0$, more sophisticated matching techniques are required.

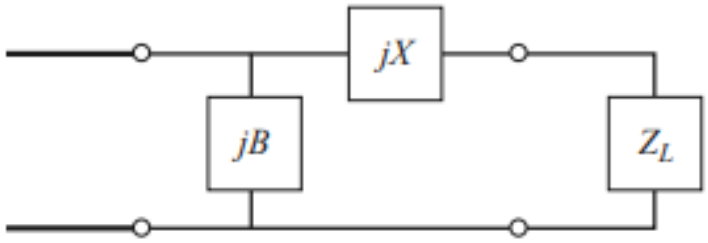

Figure 1.6: Π-Network matching for low resistance loads.

For loads with $R_L < Z_0$, a three-element matching network like the *pi* network provides enhanced impedance transformation flexibility (see fig. 1.6). The design equations are:

$$X = \pm\sqrt{R_L(Z_0 - R_L) - X_L} \tag{1.20}$$

$$B = \pm\sqrt{\frac{(Z_0 - R_L)}{R_L}} \Big/ Z_0 \tag{1.21}$$

in impedance matching networks, X represents the series reactance, while B represents the parallel susceptance. Both parameters are essential for transforming impedance characteristics and achieving precise circuit matching across various load conditions. These equations provide two potential solutions, allowing design flexibility based on specific circuit requirements.

Impedance matching can be achieved through multiple methods: impedance transformers utilize specific relationships between input and output impedances, transmission lines of calculated lengths modify electrical characteristics to match systems, and discrete components like inductors and capacitors provide precise impedance adjustment through strategic configuration.

This matching technique is particularly crucial in LNA design, where transistor input impedance often falls in the region where $R_L < Z_0$ region. By implementing π or T-networks, designers can optimize:

- Noise figure: Quantifies how much noise an amplifier adds to the signal, expressed as the ratio of input to output signal-to-noise ratio (SNR).
- Amplifier gain: Measures the increase in signal power or voltage provided by the amplifier, typically expressed in decibels (dB).
- Overall system performance

The art of impedance matching lies in balancing these competing requirements to achieve optimal circuit performance across RF applications.

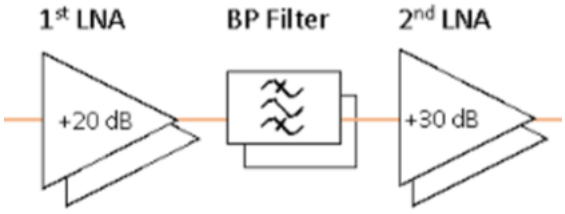

Figure 1.7: Block diagram of a front-end design. Extracted from Lin et al. 2022.

1.4.2 State-of-the-art

The design of LNA for radio astronomy applications has been thoroughly researched and continuously improved over the years, primarily due to the need to enhance sensitivity for detecting faint signals from space. This section reviews the most significant studies and solutions that have been implemented in astronomical projects with similar requirements, providing context for the development of the LNA for the CHARTS project.

BURSTT First Amplification Stage

The Bustling Universe Radio Survey Telescope in Taiwan (BURSTT) project (Lin et al. 2022) is a dedicated telescope designed to detect bright radio bursts within the 200–800 MHz frequency range. The reception front-end design consists of two amplification stages followed by a bandpass filter that selects the desired frequency band.

The first-stage LNA is integrated directly into the antenna. This design choice takes advantage of the LNA's low noise figure and excellent impedance matching. By doing so, it minimizes losses and additional noise that could arise from transmission lines connecting the antenna to the LNA.

The BURSTT front-end features an integrated LNA, a second amplification stage, and a 200–800 MHz bandpass filter. This filter eliminates unwanted signals outside the desired frequency band, enhances the SNR, and minimizes the risk of saturation in the following receiver stages.

For the specific design of the LNA, BURSTT utilized microstrip technology for impedance matching. This method employs transmission lines printed on a dielectric substrate, allowing for precise control of characteristic impedances and enabling circuit miniaturization.

The BURSTT's LNA is engineered to optimize both noise figure and gain, which are crucial for maximizing receiver sensitivity. Low-noise transistors were selected, and carefully calculated impedance matching and biasing techniques were applied to ensure optimal performance within the target frequency range.

Figure 1.8: LNA design used in the GRex project. Extracted from Weinreb & Shi 2021.

GRex Design

A significant project in radio astronomy is Galactic Radio Explorer (GRex) (Connor et al. 2021; Shila et al. 2025), which monitors bright radio bursts on a galactic scale. The LNA design for GRex incorporates innovative techniques to achieve both low noise levels and high gain.

One notable feature of the GRex LNA is the use of microstrip technology for impedance matching. This approach involves constructing transmission lines and passive components on a dielectric substrate, which allows for precise control of characteristic impedances and enables compact circuit integration.

In addition to impedance matching, the GRex LNA was meticulously designed to minimize noise and maximize gain. Low-noise transistors, along with specific biasing and stabilization techniques, enhanced performance across the relevant frequency range.

The design of the GRex LNA highlights the use of microstrip technology for impedance matching and optimizing both the noise figure and gain. These strategies facilitate the creation of a sensitive and efficient receiver capable of detecting bright radio bursts across a broad frequency spectrum.

Radio-over-fiber (RFoF)

Radio Frequency over Fiber (RFoF) is an innovative technique for transmitting analog RF signals over optical fiber, offering significant advantages for radio astronomy arrays. Developed by Lau et al., this approach leverages modified Small Form-factor Pluggable (SFP) modules to create a cost-effective, dual-channel RFoF system (see fig. 1.9).

A key feature of this method is the use of standard ethernet cables to carry differential analog RF signals. The SFP modules' high-speed data pins are matched to a $100\,\Omega$ differential impedance, making them inherently suitable for this purpose. By utilizing widely available ethernet infrastructure, the system enables the reliable transmission of RF signals over long distances with minimal signal degradation and at a fraction of the cost of traditional coaxial or specialized RF cabling.

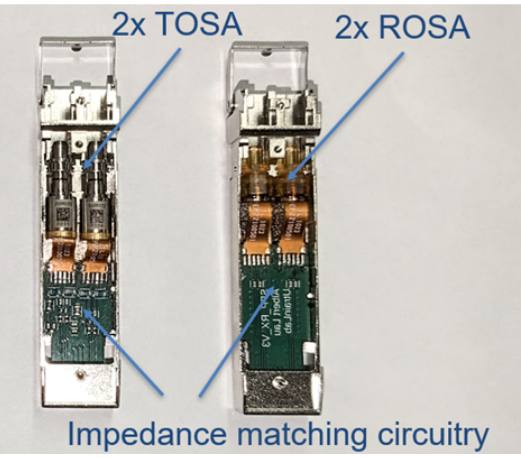

Figure 1.9: Modified SFP modules as RFoF dual channels link, where TOSA and ROSA stand for Transmitter and Receiver Optic Sub-assembly. Extracted from Lau et al. 2024.

This technology has been successfully demonstrated for transmitting RF signals over ethernet cables, achieving excellent results in terms of signal integrity and noise reduction. For the CHARTS project, RFoF presents a compelling solution for distributing analog signals from antenna arrays to centralized processing units, ensuring high-quality data transmission while maintaining scalability and cost-effectiveness.

1.5 Methods

Now, we discuss the processes involved in the design, manufacture, and characterization of the LNA, and the technical-economic assessment between the single-ended and differential implementations.

1.5.1 Design

The design process began with the use of AWR Microwave Office, an advanced electromagnetic simulation platform, to model, analyze, and optimize RF circuits.

The initial step involved surveying and comparing various commercial LNAs by evaluating their scattering parameter files (`.s2p`), as provided by manufacturers such as Mini-Circuits. After selecting the most suitable LNA, we simulated the manufacturer's evaluation board (Qorvo Inc. 2023) to validate its performance against the published specifications. Once the simulated response met the required benchmarks, the design was adapted for integration with a 50 Ohm single-ended antenna, focusing on input impedance matching within the CHARTS passband.

AWR's optimization tools were then employed to iteratively refine the circuit, enabling the exploration of alternative topologies and component values. Figures 1.10 to 1.12 illustrate key aspects of this process: the main optimization tool interface, the setup of optimization goals

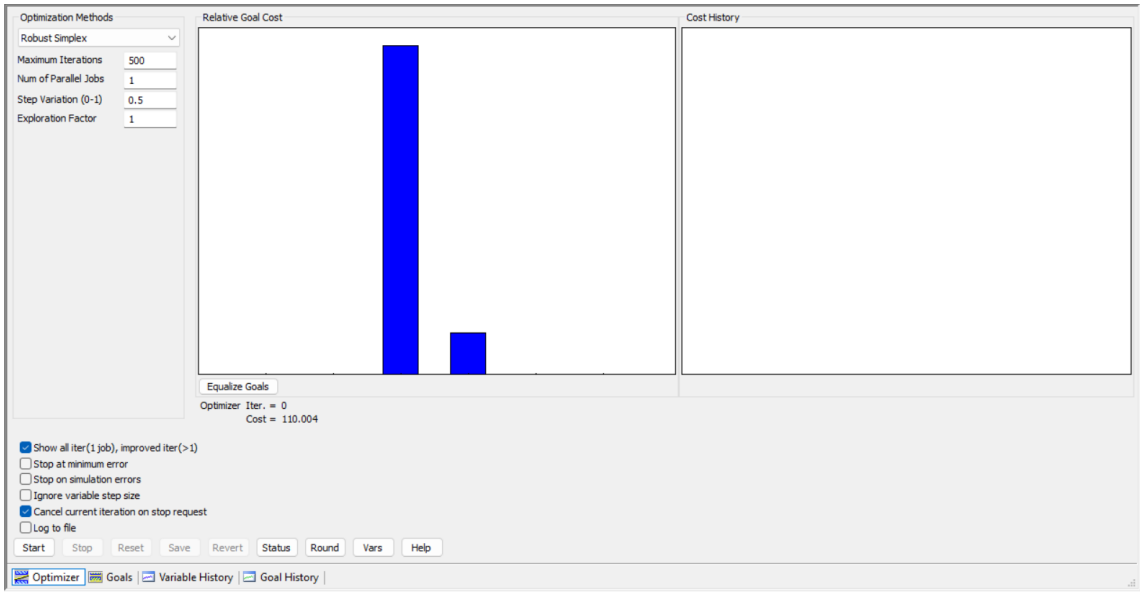

Figure 1.10: AWR optimization tool interface used for circuit refinement.

Measurement	Enabled	Cost	Weight	L	X Start	X Stop	Y Start	Y Stop	Type
TEST OS:Im(Z(1,1))	☐	0	1	2	3e+08	5e+08	0	0	Meas = Goal
TEST OS:Im(Z(2,2))	☐	0	1	2	3e+08	5e+08	0	0	Meas = Goal
TEST OS:Re(Z(1,1))	☑	97.47	1	2	300 MHz	500 MHz	50	50	Meas = Goal
TEST OS:Re(Z(2,2))	☑	12.54	1	2	300 MHz	500 MHz	50	50	Meas = Goal
TEST OS:|Z(1,1)|	☐	0	1	2	3e+08	5e+08	50	50	Meas = Goal
TEST OS:|Z(2,2)|	☐	0	1	2	3e+08	5e+08	50	50	Meas = Goal

Figure 1.11: Setup of optimization goals in AWR (e.g., gain, noise figure, reflection coefficients).

(such as target gain, NF, and reflection coefficients), and the selection of circuit parameters to optimize. These visualizations highlight the flexibility and control provided by AWR in fine-tuning the design to meet stringent requirements.

This process led to the development of new circuit layouts, which were subsequently fabricated and subjected to experimental characterization.

The simulation workflow followed a structured progression: starting from the baseline evaluation board, we first optimized the input impedance, then introduced a two-stage amplification topology to the optimized circuit. The final design incorporated both a bias tee and a dedicated input matching network to ensure optimal system integration.

This simulation-driven methodology enabled rapid evaluation of multiple circuit architectures and efficient optimization of key performance parameters—including gain, noise figure, and reflection coefficients—while minimizing development costs and reducing the need for extensive physical prototyping.

The design process culminated in the creation of a single-ended LNA that meets the

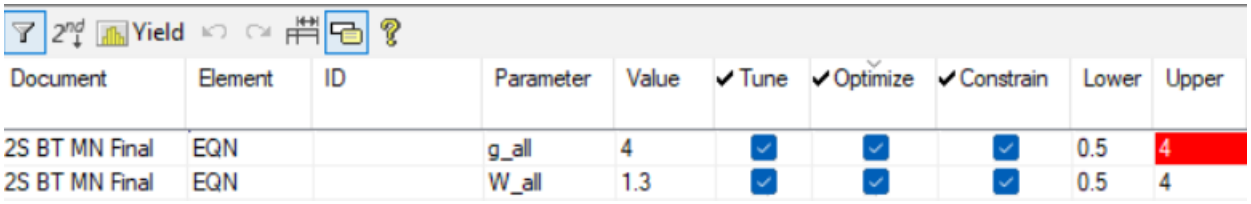

Document	Element	ID	Parameter	Value	✔ Tune	✔ Optimize	✔ Constrain	Lower	Upper
2S BT MN Final	EQN		g_all	4	☑	☑	☑	0.5	4
2S BT MN Final	EQN		W_all	1.3	☑	☑	☑	0.5	4

Figure 1.12: Selection of circuit parameters for optimization in AWR.

requirements of the CHARTS project. The final design was then prepared for fabrication, with careful consideration given to the layout and component selection to ensure optimal performance in the intended application.

1.5.2 Manufacturing

To fabricate and implement the different designs simulated, we first need to design and print a printed circuit board (PCB), and then solder the components. We used a LPKF Circuit Board Plotter for this process. Initially, we employed the Protomat S43 for drilling vias and routing the contours, fig. 1.13a, while the Protolaser S was used for laser processing, fig. 1.13b. These machines allowed us to achieve micrometric precision on the circuits produced. The material used for the fabrication of the prototypes was classic FR4. Each machine was connected to its computer to control the manufacturing process. Prototyping instructions are in chapter A.

Once the printing process is complete, the PCB needs to be reviewed and cleaned, fig. 1.13c. If there is any copper still attached to the PCB, it must be removed manually using a microscope and a scalpel. After that, we use isopropanol and a towel to thoroughly clean the PCB, preparing it for soldering.

To solder the components to the PCB, we use an Infrared Circuit Heater (ICH) T-962A to reflow-solder the components; see fig. 1.13d. This method ensures the correct soldering of the components and the proper assembly of the amplifier stage.

To use the ICH, it is necessary to adjust the heating curves to achieve optimal soldering of the components. It is important to check datasheets of the components and optimal reflow soldering curves.

1.5.3 Characterization

For the testing and characterization of the implemented circuit boards, we need to measure the scattering parameters, especially the gain and reflections coefficients (S_{21} and S_{11}), and the noise generated by the amplifier.

For the S-parameters, we use a vector network analyzer (VNA). The one used was calibrated to measure between 10–1000 GHz, this bandwidth covers the CHARTS's bandwidth (300–500 MHz). Connecting the input port to port 1 and the output to port 2 of the VNA, it

(a) Mechanic LPKF driling process.

(b) Laser LPKF process.

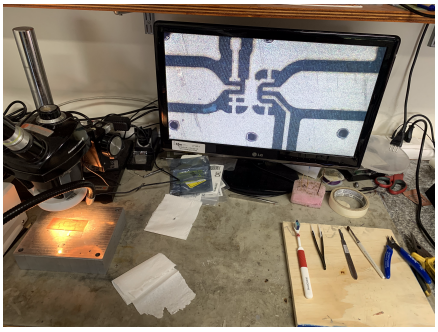

(c) Cleansing extra copper in the microstrip lines not taken by the laser process.

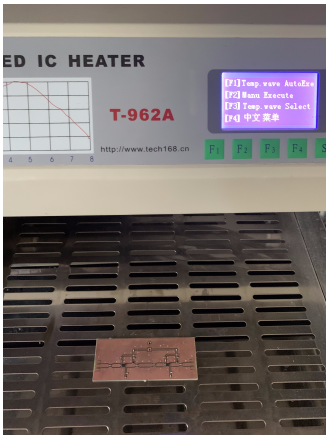

(d) Soldering process using infra-red heater and soldering paste.

Figure 1.13: PCB manufacturing steps.

was possible to measure the S-parameters and even the impedance in the input and output ports.

Noise Measurement: Y-Factor Method

The Y-factor method provides a practical approach to determining the equivalent noise temperature (T_e). This method involves measuring the system noise power when connected to two different loads: a "hot" load at temperature T_1 and a "cold" load at temperature T_2, where $T_1 > T_2$. The ratio of the noise powers, called the Y-factor (Y), is defined as:

$$Y = \frac{N_1}{N_2} = \frac{T_1 + T_e}{T_2 + T_e}$$

Here, N_1 and N_2 represent the noise powers measured for the hot and cold loads, respectively. From this, the equivalent noise temperature (T_e) of the system can be calculated using

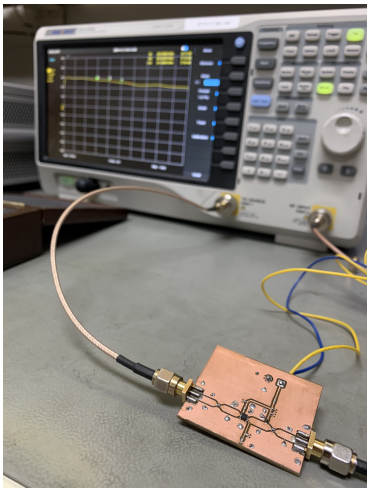

Figure 1.14: Measuring S-parameters of an iteration of the LNA using a spectral analyzer in VNA mode, in the screen of the device it is a glance of the active gain for this iteration.

the formula:

$$T_e = \frac{T_1 - YT_2}{Y - 1}$$

Steps for the Y-Factor Method

1. **Set Up the Measurement System**: Connect the DUT to a noise source capable of providing two known and distinct temperatures (T_1 and T_2).
2. **Measure Noise Powers**: Measure the system output noise power N_1 with the hot load (T_1) and N_2 with the cold load (T_2).
3. **Compute the Y-Factor**: Calculate Y as the ratio N_1/N_2.
4. **Calculate** T_e: Use the equation for T_e to determine the equivalent noise temperature of the DUT.

This method is widely used to characterize LNA and other RF systems, providing a simple yet effective means of quantifying system noise performance. Performing a hot-cold test is important to measure the noise added by the amplifier to the signal in terms of noise temperature.

To measure the noise temperature of the LNA, we employed a hot noise source with an ENR of 15.2 dB, followed by a chain of amplifiers and filters after the DUT. This chain provided an additional 34 dB of gain and bandpass filtering between 290–2750 MHz. This configuration ensures that the output signal exceeds the noise floor of the spectrum analyzer and suppresses out-of-band signals. A block diagram of the measurement setup is shown in fig. 1.15.

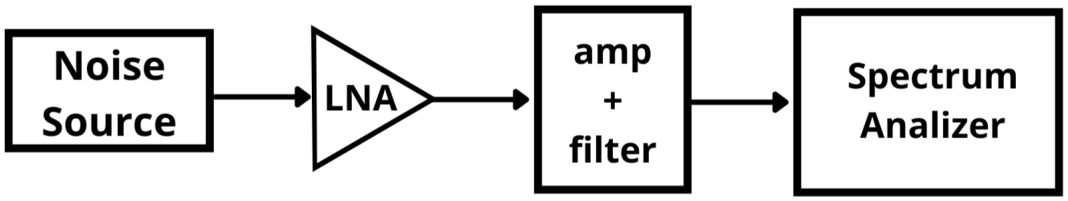

Figure 1.15: Block diagram of the experimental setup used for measuring the noise temperature of the amplifier using the hot-cold method.

The measurement procedure began by connecting the DUT to a calibrated hot noise source (see fig. 1.16a) and recording the output power using a spectrum analyzer. The hot noise source was then replaced with a cold source, and the output power was measured again. The Y-factor was calculated as the ratio of the measured output powers, enabling determination of the DUT's equivalent noise temperature using the Y-factor formula.

To accurately isolate the noise contribution of the LNA, the same procedure was performed with only the amplifier box (excluding the DUT), and the resulting noise temperature was subtracted from the total measured with the DUT in place. The complete experimental setups for these measurements—including the noise source, amplifier box, and LNA configurations—are illustrated in figs. 1.16a to 1.16d.

1.5.4 Technical-Economic Evaluation

The technical-economic comparison of the single-ended and differential LNA implementations was carried out using a clear, step-by-step approach.

First, an overview of both LNA architectures was developed, detailing their respective signal chain topologies, integration strategies, and deployment considerations within the CHARTS array. This initial analysis established the fundamental differences between the single-ended and differential approaches, particularly in terms of antenna design, LNA placement, and cabling requirements.

Next, a focused technical review was performed, with particular attention given to the differential LNA implementation. Key performance metrics—including noise temperature and gain—were measured and compared for both architectures. Laboratory setups were used to evaluate electromagnetic compatibility and susceptibility to RFI, ensuring that the assessment reflected realistic deployment conditions.

Following the technical analysis, a detailed economic evaluation was carried out. This involved compiling a cost breakdown for each implementation, including major components, PCB fabrication, and auxiliary circuitry. Special emphasis was placed on cabling costs, as the choice between coaxial and ethernet cables represents a significant economic impact at the scale of the CHARTS project. All costs were extrapolated to a full-scale deployment of 256 channels to reflect the project's requirements.

Throughout the evaluation, comparative tables and figures were generated to clearly

(a) Noise source used for hot-cold measurements.

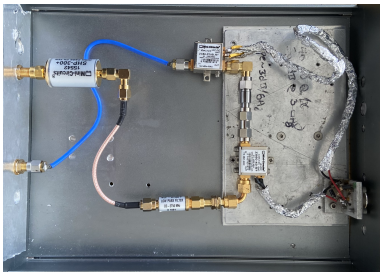

(b) Inside view of the amplifier box.

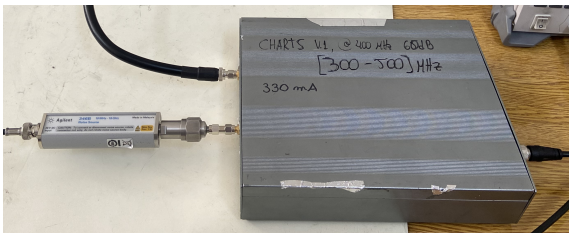

(c) Configuration for measuring the noise temperature of the amplifier box.

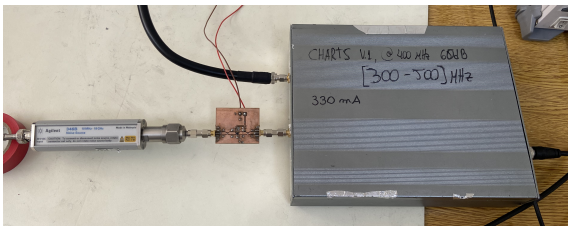

(d) Configuration for measuring the noise temperature of the LNA.

Figure 1.16: Experimental setups for noise temperature measurements: (a) noise source used for hot-cold measurements, (b) amplifier box interior, (c) amplifier box measurement configuration, and (d) LNA measurement configuration. The noise source provides a known excess noise ratio (ENR), enabling accurate determination of the device under test's noise temperature using the Y-factor method.

present the results and highlight the trade-offs between technical performance and overall system cost. This methodology ensured that the technical-economic comparison was rigorous and relevant to the selection of the optimal amplification solution for the CHARTS project.

In chapter 2 the design and implementation of the single-ended LNA will be presented, including the design process, manufacturing details, and characterization results. Chapter 3 will focus on the results of the single-ended LNA, detailing its performance. Finally, chapter 4 will provide a comprehensive technical-economic comparison between the two approaches, concluding with recommendations for the most suitable amplification solution for the CHARTS project.

Chapter 2

Design and Implementation

This chapter outlines the general design and implementation of the first amplification stage for CHARTS. It begins with the requirements and progresses to selecting the active amplification component. The simulations are then performed using AWR software, starting with the manufacturer-recommended configuration for the component test board. This is followed by an iteration that adapts the design to achieve better input impedance matching to $50\,\Omega$ and integrates two stages of amplification. Finally, the chapter presents the design and simulations for a complete system that includes a bias tee for the two-stage amplification system and an input impedance matching network.

2.1 Requirements

This section details the requirements for the project's first-stage amplifier. The various elements must work together as part of the reception chain to achieve the project's objectives.

Figure 2.1 presents a block diagram of the CHARTS front-end, which spans signal reception to the stage before digitization, including the first and second amplification stages and the 8-chains FDM. The amplification stages are essential between the antennas and the FDM due to the low power of the received signals and the distance between them.

First, the design must consider the antenna selected for the project. This is because the input of the LNA must be matched to the output impedance of the antenna (typically $50\,\Omega$). Various antenna designs have been proposed for the project, each offering different advantages and disadvantages in meeting CHARTS' overall objectives. Among the most important parameters considered are the angular width of the main beam and how the antennas perform in a 256-element array.

Two antenna designs were selected for field testing based on their comparable performance characteristics, as shown in figs. 4.2 and 4.4. Both configurations exhibit approximately 7.5 dB gain at 400 MHz. The single-ended design (fig. 2.2) demonstrates effective $50\,\Omega$ impedance matching within the 300–500 MHz target band, achieving $S_{11} < -10\,\text{dB}$ across 300–500 MHz. Similarly, the differential antenna maintains $S_{11} < -10$ dB throughout

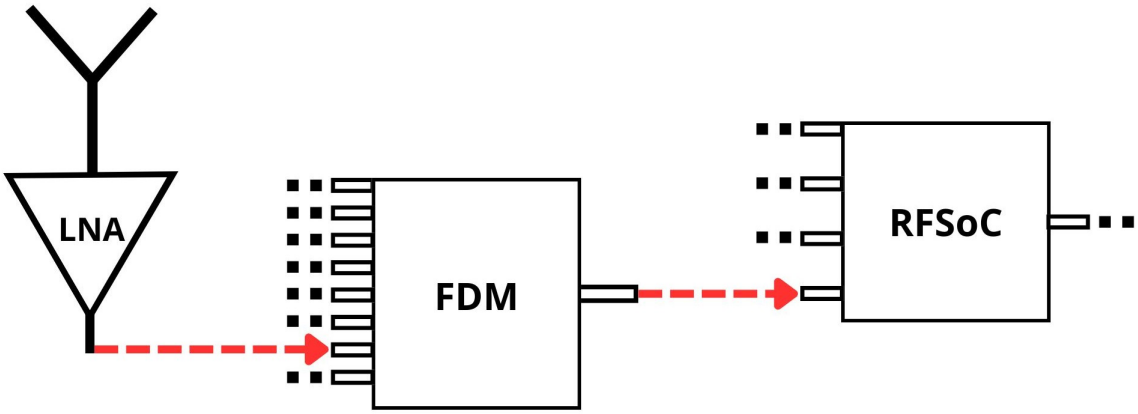

Figure 2.1: Block diagram of the CHARTS front-end reception chain. Red arrows indicate coaxial/ethernet connections between key receiver components. Only one antenna is shown for clarity.

the entire operational bandwidth, ensuring optimal power transfer for both architectures.

Amplifier design is defined by several critical performance parameters: gain, noise, and impedance. The voltage or power gain indicates the level of signal amplification, while the noise figure measures the degradation of the signal. Impedance matching, commonly at 50 Ω for single-ended configurations or 100 Ω for differential configurations, is essential to ensure efficient signal transfer and minimize power losses.

To define these requirements, a comprehensive analysis of the analog reception system is necessary. The analog chain begins at the antenna, which is directly connected to the LNA, forming the initial stage of signal amplification. From the LNA to the FDM, a 10 m coaxial cable introduces a loss of 0.89 dB (Systems 2023). The FDM itself incorporates a series of amplifiers and mixers, resulting in a net gain of 10 dB.

After the FDM, the signal is transmitted to the RFSoC via a 50 m coaxial cable, which introduces an additional loss of 4.45 dB prior to digitization. The complete analog chain for a single-ended antenna configuration is illustrated in fig. 2.1.

For simplicity and a conservative estimation of system performance, the noise temperature contributions of the FDM is considered 290 K. The RFSoC, based on the AMD–Xilinx Zynq UltraScale+ RFSoC Gen3 device, incorporates RF-ADCs with 14-bit resolution and sampling rates up to 5 GSPS (RealDigital 2024). Single-ended SMA inputs are interfaced through `MABA-011118` baluns (10 MHz–10 GHz). The ADC noise figure is estimated using the methodology of Kester (2014), employing full-scale input power, sampling bandwidth, and assumed SNR parameters.

For a full-scale differential input of $1\,V_{pp}$ (equivalent to $0.5\,V_{pp}$ single-ended), the rms voltage is

$$V_{\mathrm{FS,rms}} = \frac{0.5}{2\sqrt{2}} = 0.177\,\mathrm{V}, \tag{2.1}$$

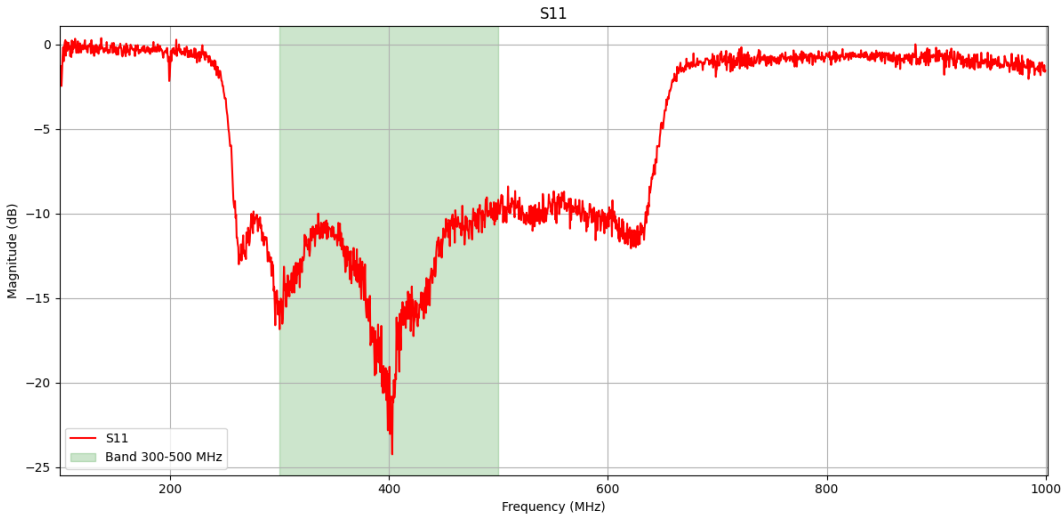

Figure 2.2: Measured return loss (S_{11}) of the single-ended antenna design across 100-1000 MHz frequency range. The highlighted band (300-500 MHz) represents the target operating frequency range, showing adequate matching performance with $S_{11} < -10$ dB for most of the band.

yielding a full-scale power across $50\,\Omega$ of

$$P_{\mathrm{FS}} = \frac{V_{\mathrm{FS,rms}}^2}{R} = 0.625\,\mathrm{mW} = -2.04\,\mathrm{dBm}. \tag{2.2}$$

At $f_s = 5\,\mathrm{GSPS}$, the Nyquist bandwidth is $B = 2.5\,\mathrm{GHz}$. The ADC noise figure is calculated as (Kester 2014):

$$\mathrm{NF} = P_{\mathrm{FS}}(\mathrm{dBm}) + 174 - \mathrm{SNR} - 10\log_{10}(B), \tag{2.3}$$

where $174\,\mathrm{dBm/Hz}$ represents the thermal noise floor. For the intended 4-bit quantization operation, the theoretical SNR limit is $\mathrm{SNR} = 6.02 \times 4 + 1.76 = 25.8\,\mathrm{dB}$. Adopting a conservative $\mathrm{SNR} = 24\,\mathrm{dB}$ to account for practical implementation losses:

$$\mathrm{NF} = -2.04 + 174 - 24 - 93.97 = 54.0\,\mathrm{dB}. \tag{2.4}$$

The corresponding noise factor $F = 10^{\mathrm{NF}/10} = 2.51 \times 10^5$ yields an equivalent noise temperature of

$$T_N = T_0(F-1) = 290 \times (2.51 \times 10^5 - 1) = 7.3 \times 10^7\,\mathrm{K}, \tag{2.5}$$

demonstrating the substantial noise contribution under reduced-resolution operation. These values, along with the gain and loss figures for each stage, are summarized in table 2.1.

To ensure optimal system performance, the receiver noise temperature must be kept below 50 K. The calculation for the total receiver noise temperature, considering the contributions from each stage, is presented below using eq. (1.7):

$$T_{rx} = T_{LNA} + \frac{T_{c1}}{G_{LNA}} + \frac{T_{FDM}}{G_{LNA}G_{c1}} + \frac{T_{c2}}{G_{LNA}G_{c1}G_{FDM}} + \frac{T_{RFSoC}}{G_{LNA}G_{c1}G_{FDM}G_{c2}} < 50\mathrm{K} \tag{2.6}$$

$$T_{LNA} + \frac{66.7}{G_{LNA}} + \frac{290}{G_{LNA} \cdot 0.81} + \frac{234}{G_{LNA} \cdot 0.81 \cdot 10} + \frac{7.3 \times 10^7}{G_{LNA} \cdot 0.81 \cdot 10 \cdot 0.36} < 50\text{K}$$

From eq. (2.6), it is clear that the noise contribution from the LNA is the most significant factor affecting the overall receiver noise temperature. Therefore, minimizing the noise temperature of the LNA is essential to achieve a low-noise system and meet the overall performance requirements. For practical analysis, the equation can be simplified as follows:

$$T_{rx} = T_{LNA} + \frac{1}{G_{LNA}} \cdot (66.7 + \frac{290}{0.81} + \frac{234}{0.81 \cdot 10} + \frac{7.3 \times 10^7}{0.81 \cdot 10 \cdot 0.36} < 50$$

$$T_{rx} = T_{LNA} + \frac{25 \times 10^6}{G_{LNA}} < 50$$

The analysis yields three critical system requirements: first, the LNA must exhibit a noise temperature below 50 K to satisfy overall system noise constraints; second, a commercial amplifier with minimum 20 dB gain is required before digitization to suppress ADC noise contribution; third, LNA gain must exceed 50 dB to ensure downstream component noise remains negligible (below 2 K).

To provide adequate safety margin and accommodate system losses, the LNA target gain is established at 50 dB. This ensures antenna signals are amplified to levels suitable for effective ADC processing, particularly critical for FRB detection where extremely weak signals demand careful amplification to avoid burial in system noise.

The first-stage amplifier noise temperature significantly impacts the overall noise chain performance, as governed by the Friis equations (eqs. (1.5) and (1.7)), necessitating minimal noise contribution. For the CHARTS project, the LNA specifications require 50 dB gain, sub-50 K noise temperature, and 300–500 MHz operational bandwidth. Precise 50 Ω impedance matching is essential to minimize signal losses and coupling effects at the antenna interface (Josaitis et al. 2022).

Table 2.1: Analog chain components considerations for noise temperature and gain objectives for the LNA design.

Stage	**Gain/Loss (dB)**	**Gain (Linear)**	**Noise Temp (K)**
Coax #1	-0.89	0.81	66.7
FDM	10	10	290
Coax #2	-4.45	0.36	234
RFSoC	-	1	7.3×10^7 K

2.2 Components Selection

2.2.1 Low Noise Amplifier Selection

To achieve the mentioned requirements, an extensive search led to a selection of LNAs that match our specifications. Table 2.2 and fig. 2.3 shows the most significant ones found and some information provided by the manufacturers (Mini-Circuits 2022, 2023a,b,c; Qorvo Inc. 2023).

As shown in table 2.2, none of the amplifiers alone achieves the required gain of 50 dB. Therefore, the proposed system must incorporate two amplification stages using one of the listed LNAs. Alternatively, a commercial amplifier could be added later in the chain, for example near the FDM, to further minimize noise contribution. The two-stage approach was chosen primarily for cost reduction, although it introduces additional design and implementation challenges. To select the most suitable amplifier, a more detailed analysis of each candidate is necessary.

Due to its higher gain in the CHARTS frequency range compared to other amplifiers, the *QPL 9547* (Qorvo Inc. 2023) was selected for designing and implementing the first amplification stage.

2.2.2 QPL 9547 & Bias Circuit

Once the IC is selected, both bias and impedance-matching circuits are needed to feed it and reduce input reflections.

The *QPL 9547* is a compact, high-linearity amplifier featuring low-noise performance in a miniature 2.2 mm surface mounted technology (SMT) package. Operating in the full CHARTS bandwidth, this device delivers a superior gain of at least 23 dB with a low noise figure of 0.5 dB, while consuming 65 mA. The amplifier supports flexible implementation with a single positive supply voltage ranging between 3.3–5 V, making it ideal for space-constrained high-performance RF applications.

The fig. 2.4 shows the schematic proposed by the manufacturer and table 2.3 specifies

Table 2.2: Key specifications of candidate LNAs for the first-stage design, including frequency range, gain, noise figure, price, and operating temperature.

Name	Operational Frequencies	Central Frequency	Gain @ Central Freq [dB]	Noise Figure @ Central Freq [dB]	Unit Price (USD $)	Operating Temperature [C]
TSS-13LN+	1 - 1000 MHz	∼350 MHz	22,8	1,1	$11,73	-40° - 105°
PHA-13LN+	1 - 1000 MHz	∼350 MHz	22.6	1	$11,96	-40° - 105°
PMA2-63LN+	400 - 6000 MHz	400 MHz	24,1	0,5	$5,05	-40° - 95°
PMA2-33LN+	400 - 3000 MHz	400 MHz	24,4	0,78	$4,54	-40° - 95°
QPL9547SR	100 - 6000 MHz	3 GHz	19,5	0,5	$6,25	-40° - 105°

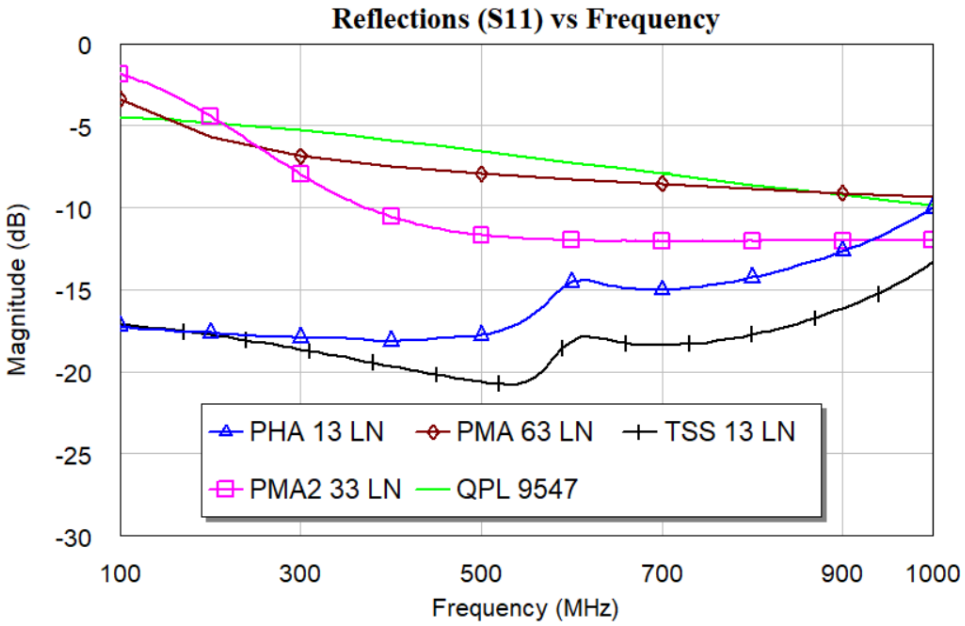

(a) S_{11} (input reflection coefficient) of candidate LNAs evaluated for the project.

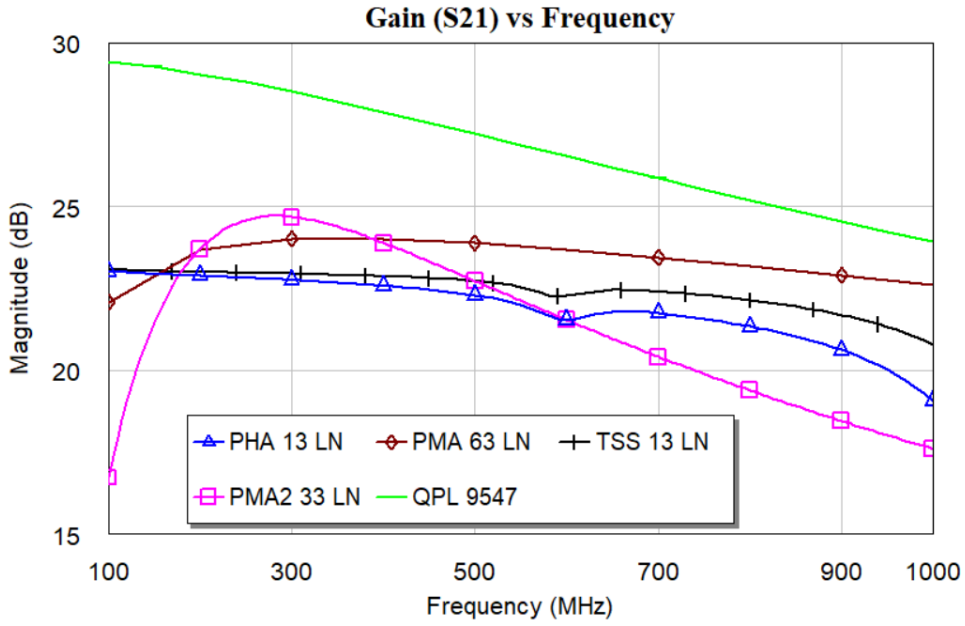

(b) Gain or S_{21} parameter of the LNAs candidates, as provided by the manufacturers' datasheets.

Figure 2.3: S_{11} and S_{21} parameters of the components presented in table 2.2.

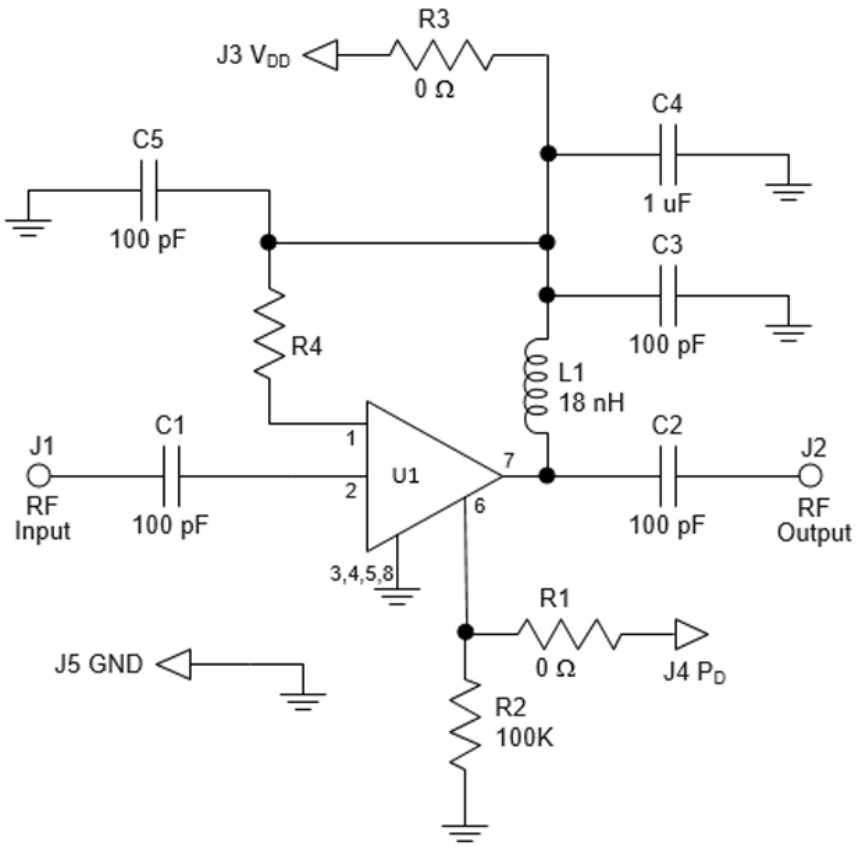

Figure 2.4: Manufacturer-recommended biasing circuit schematic for the QPL 9547 LNA, including all passive components required for optimal performance. Extracted from Qorvo Inc. 2023.

the values of the components presented in the figure. This configuration gives the nominal results presented by the manufacturer.

2.3 Design

To achieve the requirements listed previously, I've proposed a design using two stages of amplification, adding an input matching network and a bias tee at the output to feed the amplifiers. These are crucial to improve metrics such as gain and reduce reflections, and the noise temperature that the LNA adds to the receiver. The block diagram in fig. 2.5 shows the proposed design.

Several simulations were conducted to achieve the final design; using AWR software, I was able to parameterize the microstrip line values and the bias component values to optimize circuit performance.

The starting point was the design presented by the manufacturer (see fig. 2.6). The simulation of one stage of amplification in AWR are shown in fig. 2.7, where the length and

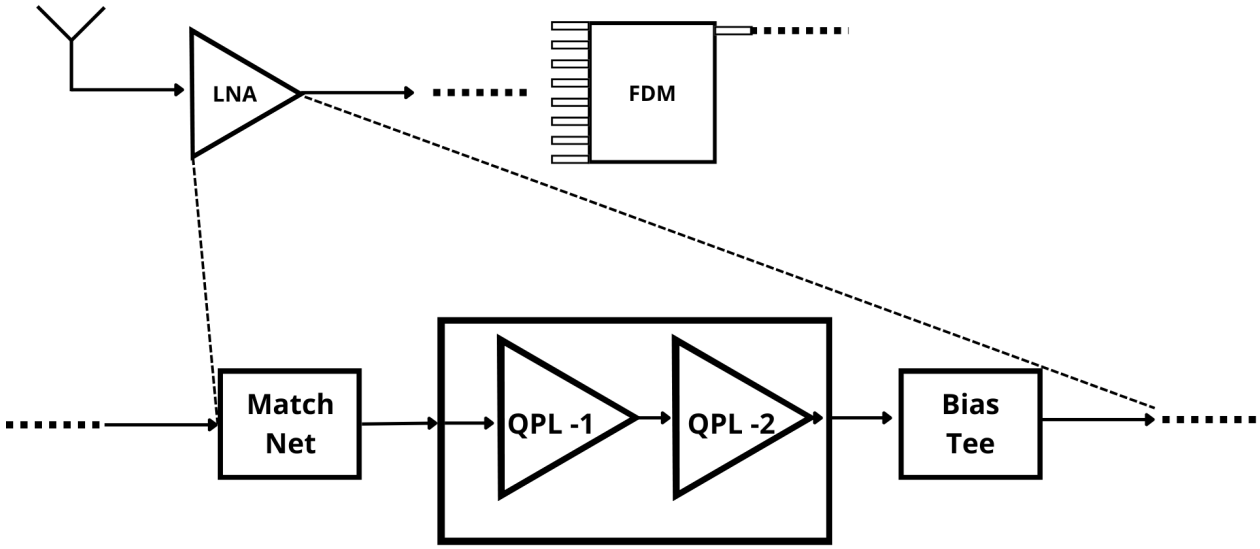

Figure 2.5: Block diagram of the proposed two-stage LNA design, including input matching network and bias tee for optimal performance in the 300–500 MHz band.

width of the microstrip lines are presented in tables 2.4 and 2.5.

The design, as mentioned earlier, includes an input impedance matching network, to adapt the input port to 50 Ω, two QPL9547 bias circuits, and a bias tee circuit at the output to power the amplifier stages (see fig. 2.8). The simulated matching network and bias tee are presented in detail in figs. 2.9 and 2.10.

The length and width of the microstrip lines for the simulation of two stages with a matching network and a bias tee are presented in tables 2.6 to 2.8. The bias circuit of each amplifier stage uses the same dimensions as the datasheet-based design; see table 2.5.

Table 2.3: Bill of materials for QPL 9547 LNA bias network implementation. Components listed follow manufacturer specifications for optimal DC operating point and RF performance. Zero-ohm resistors (R1, R3) serve as jumpers for circuit flexibility.

Component Type	Designator	Value	Quantity
Capacitor	C1, C2, C3, C5	100pF	4
	C4	1µF	1
Inductor	L1	18nH	1
Resistor	R4	3.32kΩ	1
	R2	100kΩ	1
	R1, R3	0Ω	2

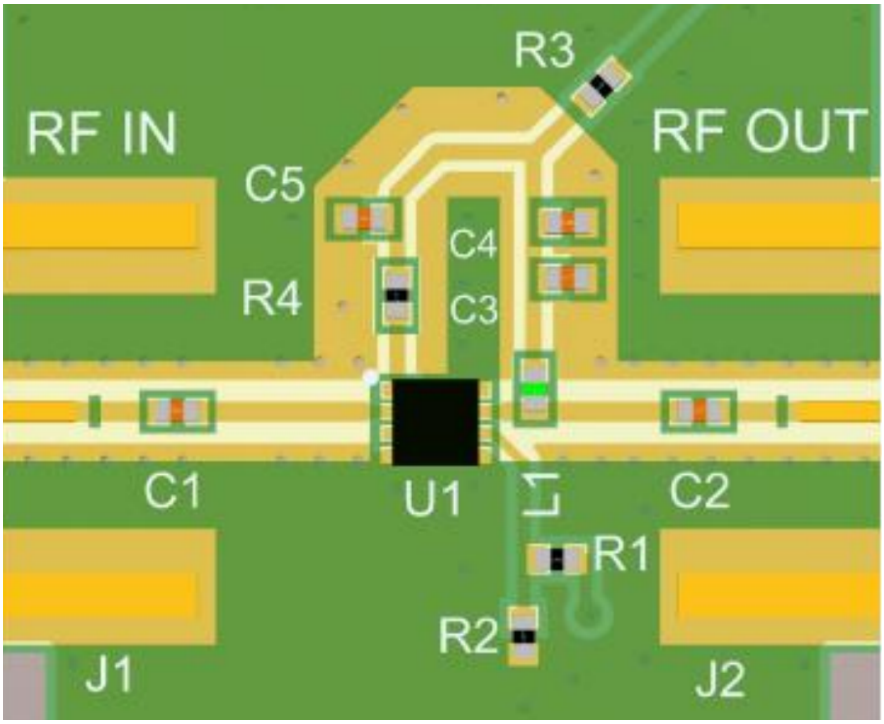

Figure 2.6: Layout of the QPL9547 test board as provided by the manufacturer, illustrating the recommended microstrip and component placement for optimal amplifier performance. Figure taken from Qorvo Inc. 2023.

It is also important to note that some of the parameters change from table 2.5 to table 2.6; L_ex, L_cen replace some of the datasheet-based parameters, this was made to achieve symmetry in the circuit, to balance the impedance at both input and output ports.

The final modification to the manufacturer's design was the inductor in the bias circuit. The simulation results in AWR software improve when using a 2000 nH inductor, which is the same value used in the bias tee.

Figures 2.7 to 2.10 illustrate the layout of each component (white blocks) and the coplanar waveguides as parameterized in the software (hatched blocks). Implementing these detailed models yields results that more closely match the physical behavior of the circuit.

2.4 Implementation

The implementation of the designed circuit requires a sequence of critical steps. First, all required components must be procured, ensuring that specifications and quality standards are met. Next, the PCB must be carefully designed with appropriate routing prior to fabrication. Following production, all components must be precisely soldered to the board using the ICH, with a heat curve selected accordingly.

This section presents the implementation process in detail, covering component selection, PCB design considerations, manufacturing specifications, and assembly procedures to ensure

Table 2.4: Principal microstrip line dimensions for input and output matching networks in the datasheet-based LNA design. All dimensions correspond to physical lengths on the PCB substrate.

Parameter	**Size (mm)**
L_in_1	2.4
L_in_2	1
L_out_1	0.8
L_out_2	2
L_out_3	2
W	0.6
GAP	0.6
W_c	0.4

Table 2.5: Microstrip line dimensions for the bias network implementation in the datasheet-based amplifier design. Parameters with 0.001 mm values represent negligible transmission line segments for circuit analysis.

Parameter	**Size (mm)**
L_c	1.5
L_c_2	1.5
L_c_3	0.001
L_c_4	0.001
L_c_5	6.7
L_c_6	1
L_c_7	0.001
L_c_8	0.001
L_c_9	0.001
L_c_10	0.001

optimal circuit performance and reliability.

To implement the designed solution, the process began with the acquisition of the various components required for the circuit. Table 2.9 presents the selected components, including supplier information and associated costs.

After purchasing the components, a PCB was designed and printed to test the simulated designs and implement the circuit. For this purpose, KiCad software was used, as it allows for comprehensive circuit board design according to the required specifications. The design is presented in fig. 2.11. To achieve this, the simulated lengths and widths from tables 2.6 to 2.8 were followed.

After designing the PCB, the printing phase follows. This involves using a standard FR4 substrate and the LPKF machine at the MWL. Following the process illustrated in fig. 1.13, a PCB can be produced that is ready for testing once all components and connectors have been soldered into place (see section 2.4). The instructions for using the LPKF machine are presented in chapter A.

Finally, to fully implement the amplifier, it is important to enclose it in a conductive case forming a Faraday cage to prevent interference from RFI. Key requirements for the enclosure include: proper electromagnetic shielding using conductive materials (metal or metallized plastic), adequate thermal management for heat dissipation, mechanical compatibility with the PCB and connectors, and effective electrical grounding between the enclosure and circuit to maximize shielding effectiveness. The prototype was 3D printed using PLA and covered with aluminium tape to perform concept tests. The final PCB sent to a manufacturer is shown in section 2.4. Components were soldered using the ICH shown in fig. 1.13d.

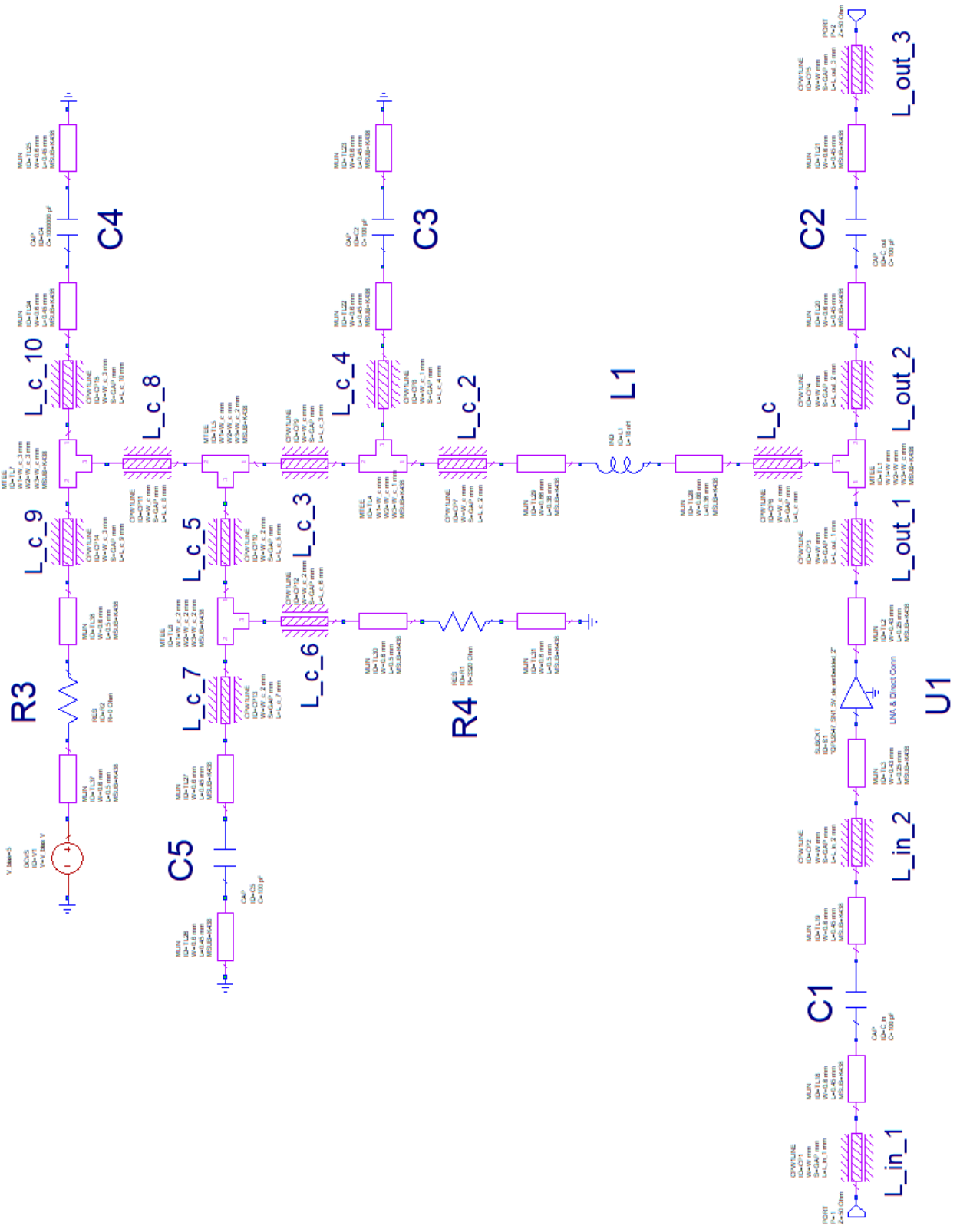

Figure 2.7: AWR simulation of the single-stage amplifier circuit, showing the layout and microstrip line dimensions as specified in tables 2.4 and 2.5.

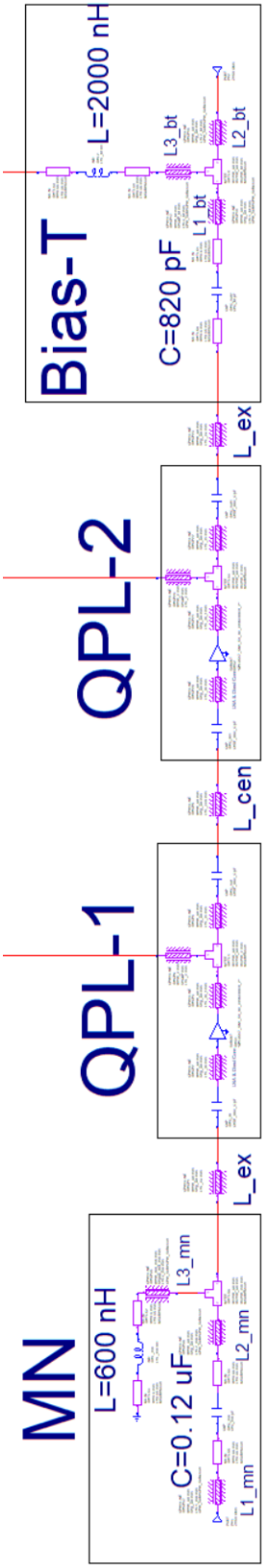

Figure 2.8: AWR simulation of the complete amplifier design, showing the integrated input matching network, two-stage amplification, and output bias tee for optimal performance across the 300–500 MHz band.

Table 2.6: Principal line lengths and widths for both amplification stages.

Parameter	Size (mm)
L_in_2	5
L_ex	5
L_out_2	1
L_cen	1
L_out_1	1
W_all	1.3
g_all	4

Table 2.7: Matching network microstrip line lengths

Parameter	Size (mm)
L1_mn	0.001
L2_mn	1.5
L3_mn	0.001

Table 2.8: Bias-T microstrip line lengths.

Parameter	Size (mm)
L1_bt	5
L2_bt	5
L3_bt	0.1

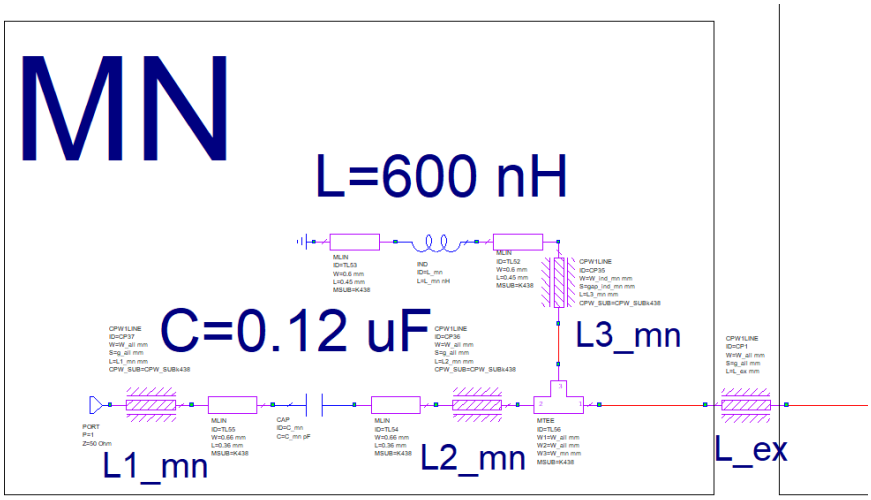

Figure 2.9: AWR simulation schematic of the input matching network, showing microstrip layout and component placement for optimal impedance matching at 50 Ω across the CHARTS band.

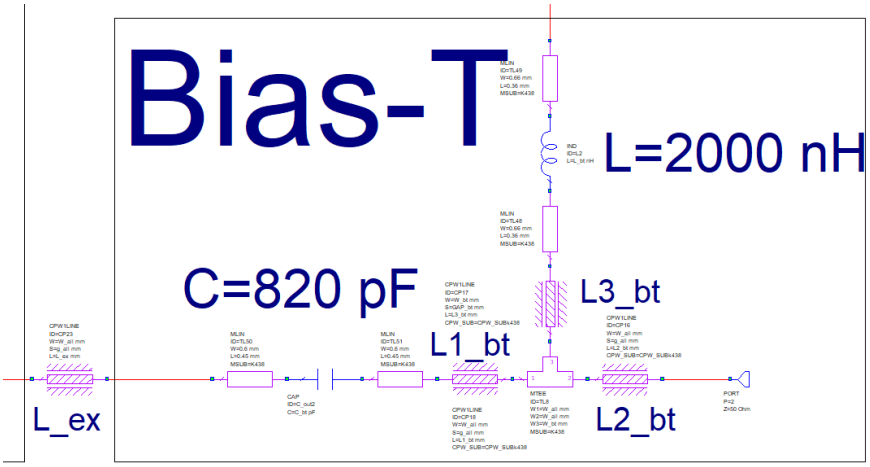

Figure 2.10: AWR simulation schematic of the bias tee circuit, showing microstrip layout and component placement for optimal DC biasing and RF isolation in the amplifier design.

Table 2.9: Component list for the two-stage amplifier: includes manufacturer-recommended parts for the QPL9547 LNAs implementation, passive elements for the input matching network, and bias tee. Seller codes, values, and quantities are specified. Total cost: $40.67.

Circuit	Type	Seller Code	Value	Qty
Bias QPL 9547	LNA	772-QPL9547TR7	-	2
	Capacitor	81-GRM1555C1H101JA1D	100pF	8
	Capacitor	81-GRT155C81E105KE3D	1uF	2
	Inductor	81-LQW15CA2R0K00D	2uH	2
	Resistor	710-560112110102	3.32kOhm	2
	Resistor	710-560112110019	100kOhm	2
	Resistor	667-ERJ-U020R00X	0 Ohm	4
Impedance Matching	Capacitor	81-GRM155R61A124ME9D	0.012uF	1
	Inductor	994-0402HL-601XJRW	0.6uH	1
Bias Tee	Capacitor	81-GCM1555G1H821JA6D	800pF	1
	Inductor	81-LQW15CA2R0K00D	2uH	1

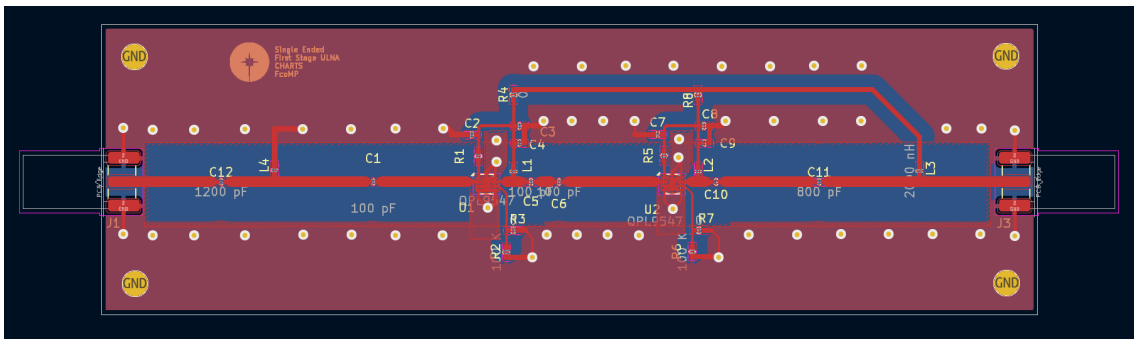

Figure 2.11: Final two-stage amplifier PCB layout designed in KiCad, sent to a specialized manufacturer for fabrication.

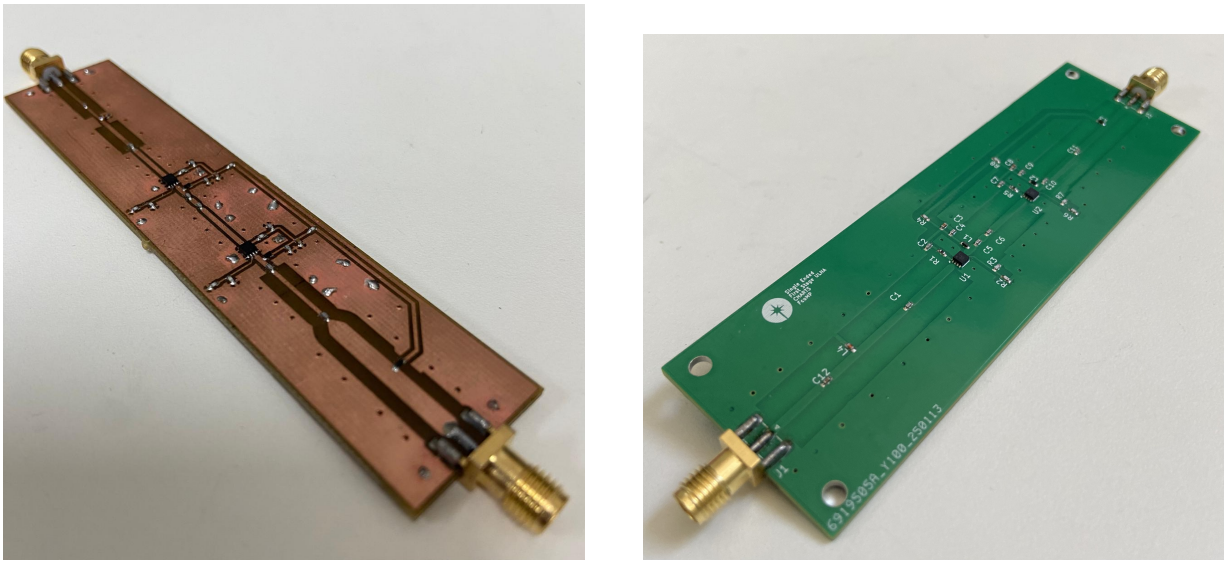

Figure 2.12: Prototype and final PCB for the two-stage amplifier: (a) initial prototype fabricated and assembled using the LPKF milling machine, assembled for initial testing and validation of the amplifier design; (b) final manufactured board printed by a specialized manufacturer, and soldered by using an ICH. This is the final PCB used for the tests.

Chapter 3

Single-Ended LNA Results

This chapter presents the results of the tests performed on the single-ended LNA system. The following sections detail the measured scattering parameters and noise temperature across the relevant frequency bands.

3.1 Scattering Parameters

The measured scattering parameters of the single-ended LNA system are shown in fig. 3.1, S_{21} and S_{11}, referred to as gain and reflections, respectively. Figures 3.1b and 3.1d focuses on the CHARTS operational band. The results show excellent gain performance, with S_{21} reaching values even higher than the design target at some frequencies: 56 dB at 300 MHz, 54 dB at 400 MHz, and 50 dB at 500 MHz.

Now, in figs. 3.1a and 3.1c, the gain and reflection performance across the full testing band, which spans 10–1000 MHz, can be seen. A notable peak appears at approximately 200 MHz in fig. 3.1a, corresponding to the resonance frequency of the 2000 nH inductor. This should not affect the overall amplifier performance within the desired band but may produce some standing waves and/or harmonics in the system.

The reflections, represented by S_{11} in figs. 3.1c and 3.1d, are higher than the simulated results, indicating that the input matching is acceptable but could be improved. However, in fig. 3.1d the reflection coefficient S_{11} remains just below -3 dB throughout the band, which, while acceptable, does not fully meet the ideal objective of achieving lower reflection (e.g., $S_{11} < -10$ dB).

The discrepancy between simulated and measured S_{11} is primarily attributed to manual soldering imperfections using an ICH, which can introduce variations in component placement and solder joint quality. Professional fabrication with controlled reflow soldering processes would likely yield results closer to the simulation, as it ensures more precise component positioning and consistent solder joint characteristics.

In figs. 3.2a to 3.2c, the simulated and measured input and output impedances of the

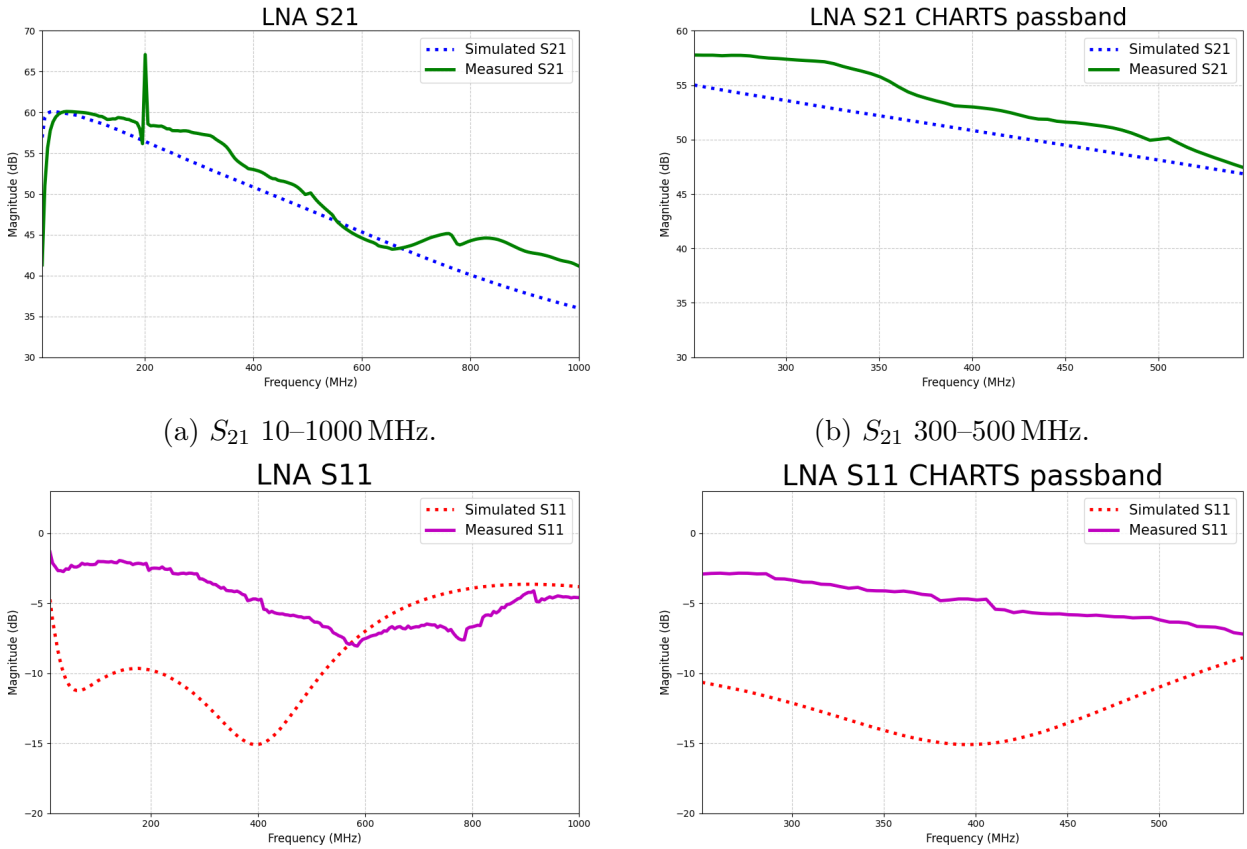

(a) S_{21} 10–1000 MHz.

(b) S_{21} 300–500 MHz.

(c) S_{11} 10–1000 MHz.

(d) S_{11} 300–500 MHz.

Figure 3.1: Measured S_{21} (gain) and S_{11} (reflection) parameters of the single-ended LNA final design. Top: S_{21} for the full testing band and the CHARTS passband. Bottom: S_{11} for the full testing band and the CHARTS passband.

LNA are presented.

The markers in fig. 3.2a indicate the simulated input and output impedances of the LNA at 400 MHz, with a reference impedance of $Z_0 = 50\,\Omega$. The simulated input impedance at 400 MHz is (42.6-43.4j) Ω, while the output impedance is (50.2+4j) Ω (markers m2 and m1 in fig. 3.2a, respectively). The measured input impedance in fig. 3.2b shows a value of (72.34-46.96j) Ω at 400 MHz, which is close to the simulated imaginary component but exhibits a significant 30 Ω difference in the real part.

For the output impedance measured in fig. 3.2c, the value at 400 MHz is (25.49-6.14j) Ω, which differs from the simulated value of (50.2+4j) Ω at the same frequency. The real part shows a difference of approximately 25 Ω, while the imaginary part differs by about 6 Ω. This indicates that the input and output matching is not optimal but not far from what the simulations predict. However, for perfect matching, we would expect the input and output impedances to be closer to 50 Ω with the imaginary parts closer to zero.

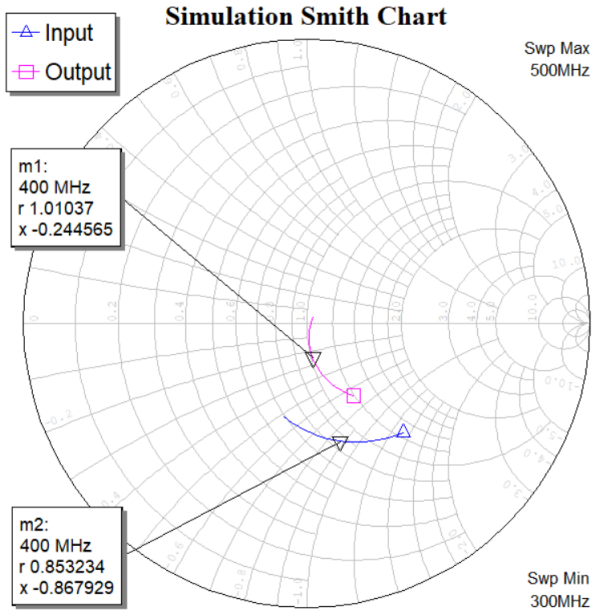

(a) Simulated input and output impedances of the LNA across CHARTS band of interest, $Z_0 = 50\,\Omega$.

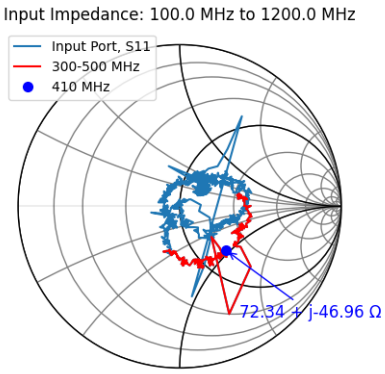

(b) Measured input impedance of the LNA, marked in red the CHARTS band of interest.

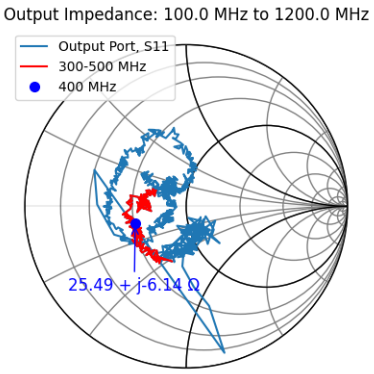

(c) Measured output impedance of the LNA, marked in red the CHARTS band of interest.

Figure 3.2: Simulated and measured impedance results for the LNA: (a) simulated input and output impedances, (b) measured input impedance, and (c) measured output impedance. These plots provide insight into the matching performance of the LNA at both ports.

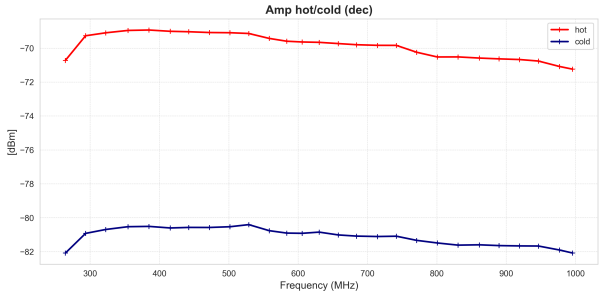

(a) Hot-cold data acquisition for the amplifier box.

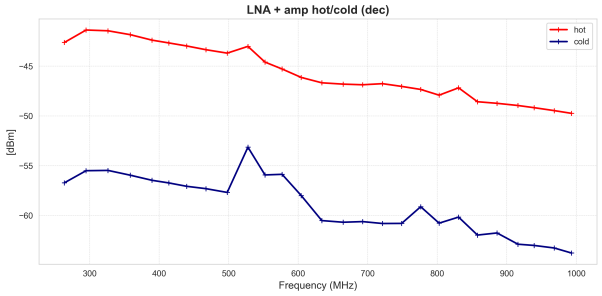

(b) Hot-cold data acquisition for the amplifier box and LNA (DUT).

Figure 3.3: Hot-cold data acquisition for (a) the amplifier box and (b) the amplifier box with LNA (DUT). "Dec" indicates decimated data, where the number of points was reduced by integrating the measured power to improve measurement accuracy.

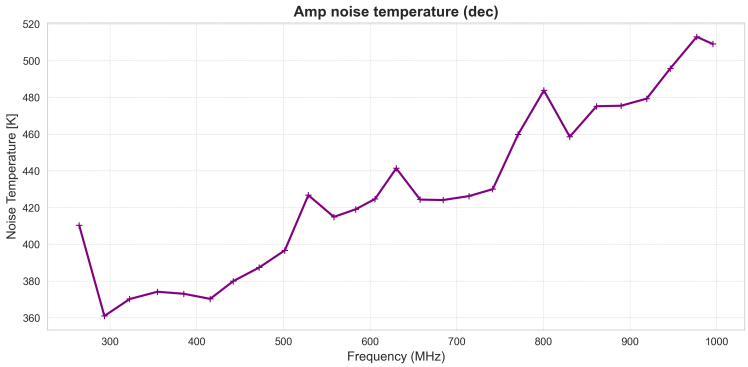

Figure 3.4: Amplifier box noise temperature.

3.2 Noise Temperature

The noise temperature measurements were performed using the hot-cold method, which involves acquiring the output power spectrum of the system when exposed to two known reference temperatures (hot and cold loads). This process allows for the calculation of the system noise temperature by comparing the measured power levels. Figures 3.3a and 3.3b show the data acquisition for the "amplifier box" alone and for the "amplifier box" plus LNA (DUT), respectively.

The noise temperature of the amplifier box alone is shown in 3.4. The measured noise temperature varies between 380–400 K across the CHARTS band of interest (300–500 MHz).

The principal and most valuable result is presented in fig. 3.5, which shows the measured noise temperature of the LNA within the CHARTS band. The noise temperature is higher than expected, at 70 K, and this degradation is attributed to the input reflections discussed in the S-parameter section. The insufficient input matching, as evidenced by the S_{11} values shown in figs. 3.1c and 3.1d and the input impedance mismatch in fig. 3.2b, leads to an increased noise figure due to signal reflections.

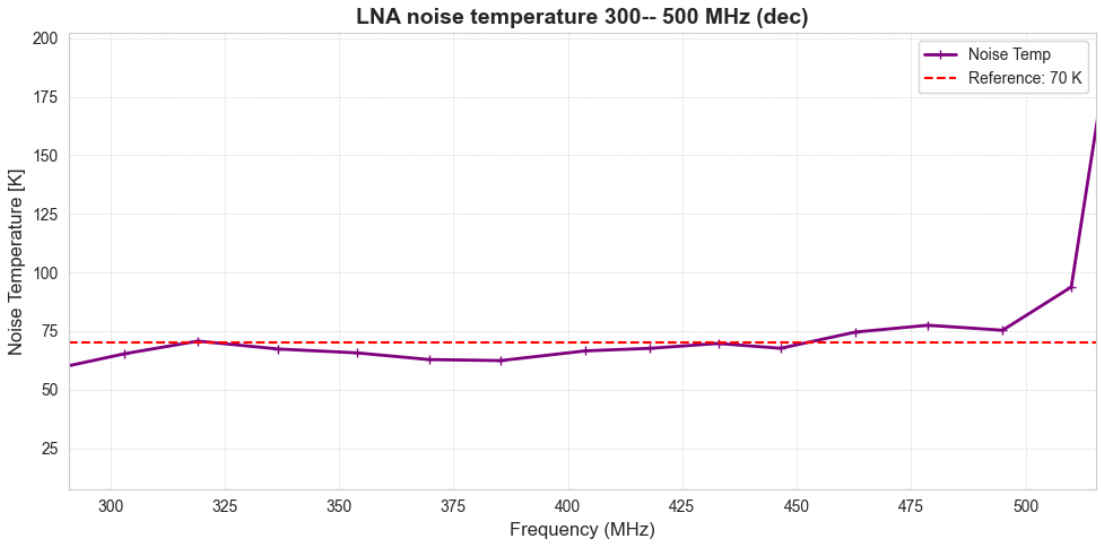

Figure 3.5: LNA noise temperature in the CHARTS band. The 70 K noise temperature is attributed to input reflections and poor matching. "Dec" indicates decimated data, where the number of points was reduced by integrating the measured power to improve measurement accuracy.

Chapter 4

Techno-Economic Comparison of Single-Ended vs. Differential LNA Implementation

This chapter provides a detailed review and comparison of single-ended and differential LNA systems, emphasizing both technical and economic considerations. The analysis addresses implementation details, key performance metrics such as gain, reflection coefficients, and noise temperature, as well as a comprehensive cost breakdown extrapolated to a full-scale deployment (256 elements). The results offer practical guidance for advancing the objectives of the CHARTS project.

4.1 Overview of Single-Ended and Differential LNA Systems

To identify the optimal front-end architecture for the CHARTS project, a direct comparison between single-ended and differential implementations is necessary. Both approaches share a similar high-level structure—which comprises an antenna, an LNA, and a FDM—but differ significantly in signal chain topology and integration strategies.

In the single-ended configuration, a $50\,\Omega$ printed antenna is employed, with the LNA mounted directly at the antenna feed point to minimize signal loss and external noise pickup. The amplified signal is routed via coaxial RF cable to a bias tee which supplies the required direct current (DC) bias, and then to the FDM. All interconnections require coaxial RF cables (e.g., LMR-400 Systems 2023), increasing both complexity and cost, particularly for large-scale arrays. fig. 4.1 presents the block diagram, while fig. 4.2 illustrates the antenna and its integration with the LNA.

The differential implementation utilizes a $100\,\Omega$ differential antenna with the LNA directly integrated at the feed point. This configuration enables immediate amplification, reducing noise pickup and losses. A key advantage is the use of standard ethernet cables for the

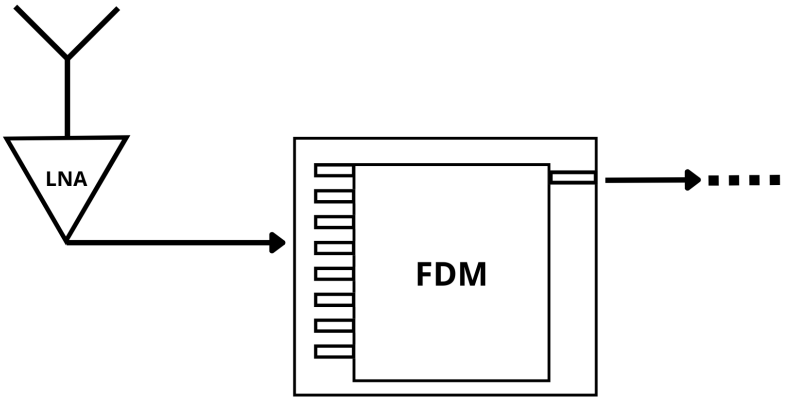

Figure 4.1: Block diagram of the analog single-ended signal chain for one antenna only, includes: the differential antenna, LNA, coaxial cable, bias-tee (assembled with the FDM), and FDM. These are the main components of the single-ended LNA architecture. The RFSoC module is located 50 m from the FDM.

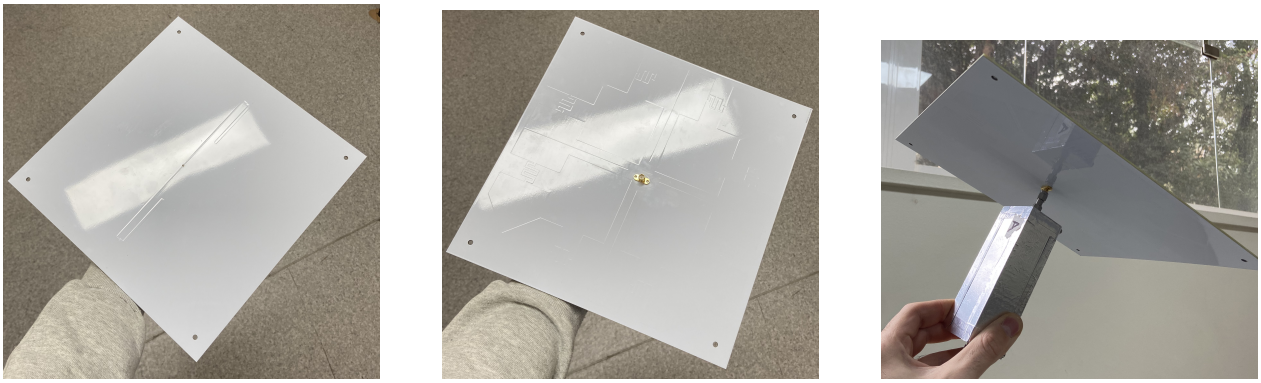

(a) Top view (b) Bottom view (c) Connected to LNA.

Figure 4.2: Single-ended printed antenna: (a) top view, (b) bottom view, and (c) connected to the single-ended LNA. These antenna has only one polarization, its connected by asma female connector to the LNA. To support the antenna + LNA a 3D-printed structure was designed, theese are not shown in the figure and its beyond of the scope of this work.

connection between the antenna-LNA assembly and the second-stage amplifier/FDM, which significantly reduces cabling costs and simplifies deployment.

Additional features, such as calibration or environmental sensors, can be integrated at the antenna. The amplified differential signal is transmitted via ethernet cable to a second-stage amplifier (with bias tee), and then to the FDM. fig. 4.3 presents the block diagram, and fig. 4.4 shows the physical realization.

It is important to note that both implementations assume the FDM and either the second-stage amplifier (differential case) or the bias tee (single-ended case) are located 10 m from the antenna. Furthermore, the RFSoC module is positioned 50 m from the FDM. These distances are consistent with the CHARTS deployment scenario, in which the antenna array is distributed over a large area.

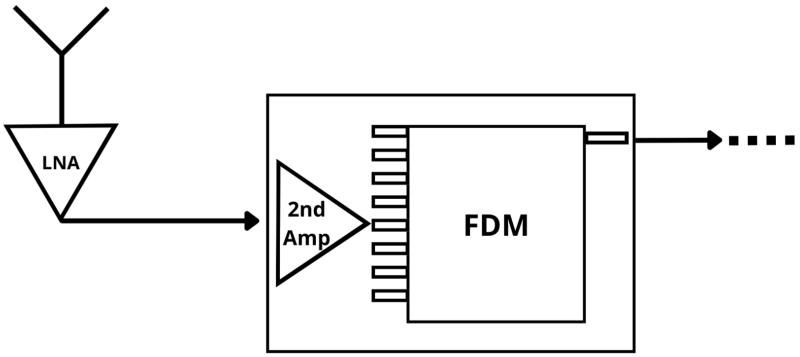

Figure 4.3: Block diagram of the analog differential signal chain for one antenna only, includes: the differential antenna, LNA, ethernet cable, second-stage amplifier with bias tee (assembled with the FDM), and FDM. These are the main components of the differential LNA architecture. The RFSoC module is located 50 m from the FDM.

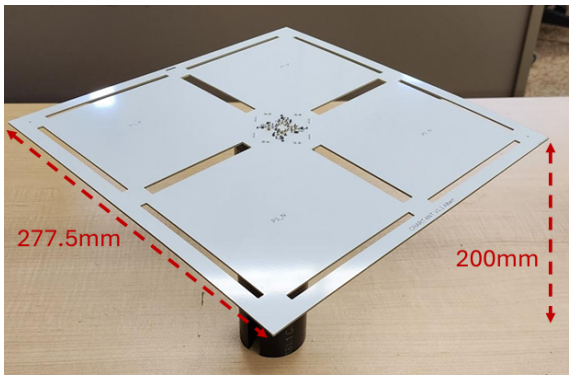

Figure 4.4: Differential printed antenna with integrated LNA at the center of the antenna. The antenna has two polarizations, each connected to the LNA,but only one it used during testing. The antenna is supported by a 3D-printed structure (not shown) to hold the antenna in place.

Electromagnetic compatibility and RFI susceptibility were evaluated using dedicated laboratory setups for each architecture. For the single-ended implementation, the setup (fig. 4.5) includes the antenna (1), LNA (2), bias tee (3), FDM with balun (4), RFSoC module (5), spectrum analyzer (6), and voltage generator (7). This arrangement closely replicates the intended deployment, enabling realistic RFI assessment.

The differential implementation was tested using a similar setup (fig. 4.6), including the differential antenna (1), LNA in an aluminum enclosure on top of the antenna itself (2), the second-stage amplifier (3), passband filter (4), balun (5), RFoC spectrometer (6), and voltage generator (7). This ensures all critical elements are included in the RFI tests.

The results demonstrate that both architectures achieve comparable performance, confirming that either approach can satisfy electromagnetic compatibility requirements. While a detailed study of RFI mitigation is beyond the scope of this work, both options remain viable.

As shown in fig. 4.7, both architectures share similar power spectrum results for the

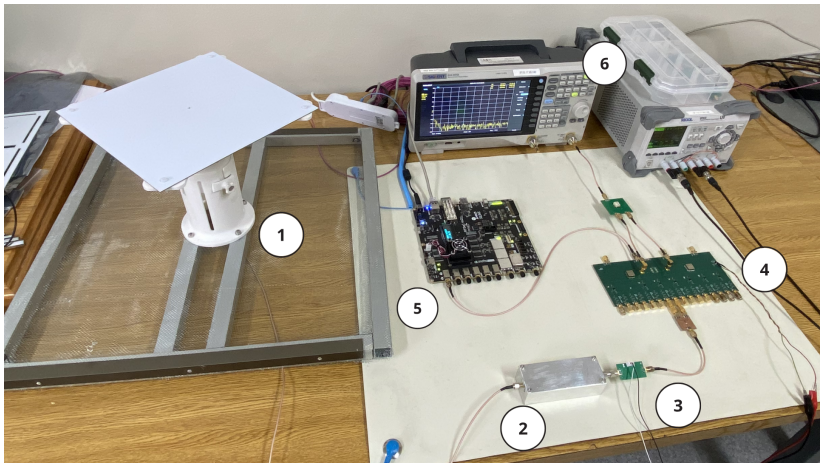

Figure 4.5: Experimental setup for evaluating RFI susceptibility in the single-ended LNA architecture. Components include: (1) antenna, (2) LNA, (3) bias tee, (4) FDM with balun, (5) RFSoC module, (6) spectrum analyzer, and voltage generator. This configuration closely simulates the actual deployment environment, ensuring representative RFI performance assessment.

CHARTS band, with the differential exhibiting higher power. Regarding functional structure, their implementation details—particularly in antenna design, LNA integration, and signal routing—lead to distinct advantages and trade-offs. This overview establishes a foundation for the subsequent technical and economic analyses.

4.2 Technical Overview of the Differential Signal Chain

This section compares a key technical parameter—noise temperature—for both single-ended and differential LNA implementations. Although the differential amplifier exhibits lower gain across the CHARTS band compared to the single-ended design, this limitation is compensated by a second-stage amplifier in the differential chain.

In the differential architecture, amplification is distributed across two stages: the first-stage differential LNA (at the antenna feed point) provides approximately 24 dB of gain, complemented by a second-stage amplifier adding approximately 22 dB. The combined gain compensates for transmission path losses and ensures the overall system meets low-noise, high-sensitivity requirements.

Figure 4.8 shows the measured system noise temperature for the differential LNA. The LNA contributes approximately 30–35 K, the antenna about 10–15 K, and the remaining approximately 5 K is attributed to the analog chain after the LNA. These results confirm that the differential LNA, together with the antenna and analog chain, provides a low-noise front-end suitable for CHARTS requirements.

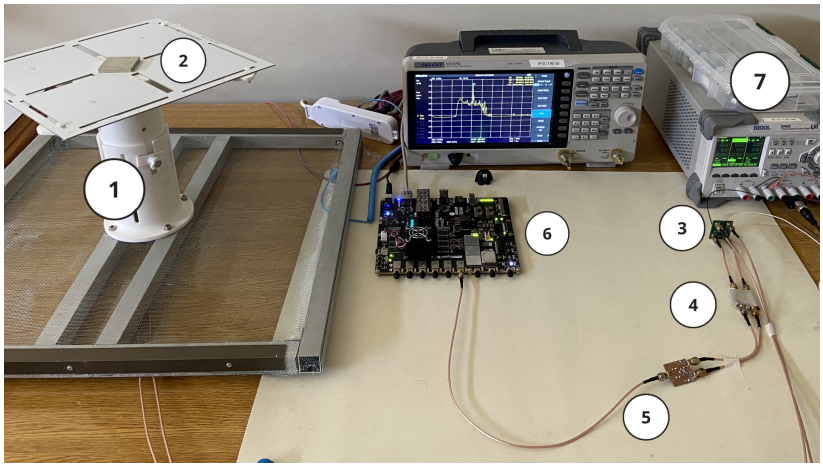

Figure 4.6: Experimental setup for evaluating RFI susceptibility in the differential LNA architecture. Components include: (1) differential antenna, (2) LNA housed in an aluminum enclosure mounted on the antenna, (3) second-stage amplifier, (4) passband filter, (5) balun, (6) RFSoC, and (7) voltage generator. This configuration closely simulates the intended deployment environment, ensuring representative RFI performance assessment.

Table 4.1: Cost breakdown for single-ended and differential analog amplification chains (per channel).

Chain Element	Component	Single-Ended (USD)	Differential (USD)
Antenna	–	50	50
LNA	QPL9547 (4)	50	50
2nd Stage Amp	AP2120N	–	1
	PSA4-5043+ (2)	–	2
Others	Passive components	7	15
PCB	–	10	15
Total		**115**	**125**

4.3 Economic Analysis

This section presents an economic comparison of the single-ended and differential LNA implementations, focusing on component and cabling costs for a full CHARTS deployment.

In table 4.1, the total cost per amplification chain is similar for both implementations, with only a minor difference of approximately $\sim$ \$10 per channel. Scaling to the full CHARTS array (256 elements), this difference amounts to \$2,560. However, this is negligible compared to the overall system costs once cabling and integration are considered.

Differential signaling enables the use of standard ethernet cables (Lau et al. 2024), which are significantly less expensive than the coaxial cables required for single-ended systems (Amazon 2024; Electronics 2024).

Table 4.2 highlights that coaxial cabling is nearly an order of magnitude more expensive than ethernet cabling. This difference becomes especially significant at the scale of the

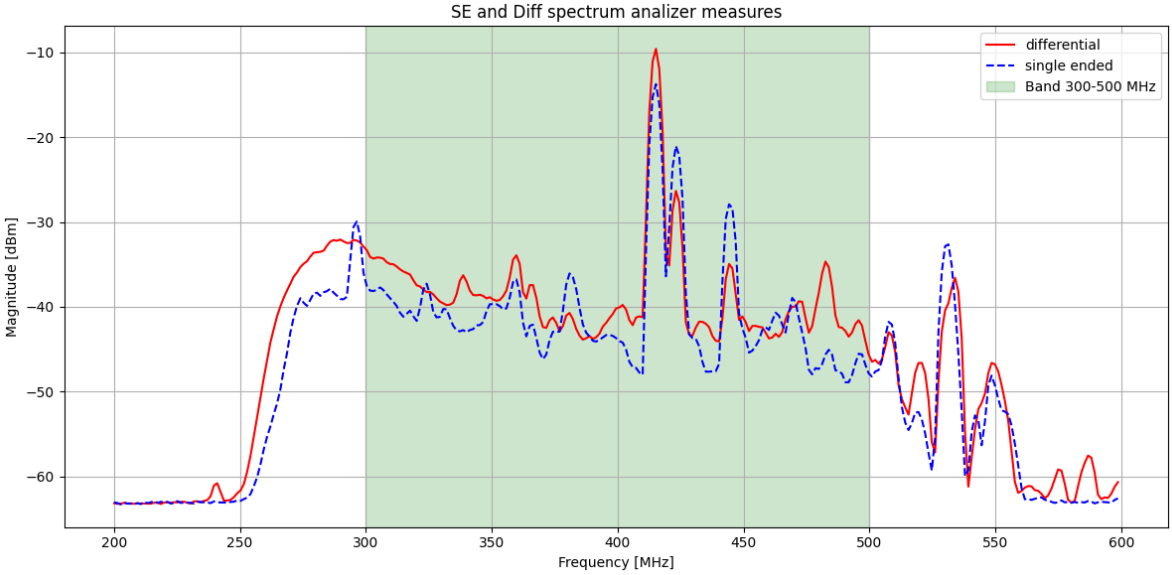

Figure 4.7: Measured power spectra for both single-ended and differential LNA configurations, illustrating comparable performance across the CHARTS frequency band.

Table 4.2: Cable cost comparison for a 50-meter run: LMR-400-FR coaxial (single-ended) vs. Cat6 ethernet (differential).

Cable Type	**Cost (USD, 50 m)**
LMR-400-FR (coaxial)	411
Cat6 ethernet	53

CHARTS project, where 256 analog channels will be implemented—one for each antenna-to-FDM connection.

As shown in table 4.3, the total cabling cost per channel is $34,195 for the single-ended implementation, compared to only $15,863 for the differential architecture. This difference offsets the slightly higher cost of the differential amplification chain, making the differential implementation nearly half the price of the single-ended solution when considering total system costs.

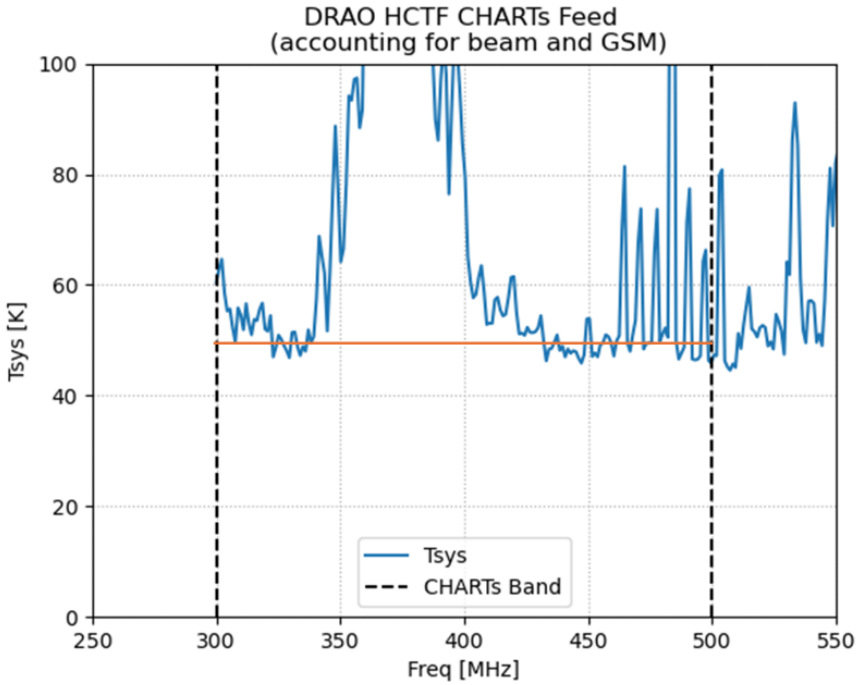

Figure 4.8: Measured system noise temperature for the differential LNA implementation. These were tested at Dominion Radio Astrophysical Observatory (DRAO) in BC Canada by CHARTS collaborator Dr. Lau.

Table 4.3: Comparison of cabling costs per channel for single-ended and differential implementations. The improvement in cost efficiency is evident, with the differential architecture significantly reducing total cabling expenses.

Implementation	**Antenna–FDM (10 m)**	**FDM–RFSoC (50 m)**	**Total (USD)**
Single-ended	21,043	13,152	34,195
Differential	2,711	13,152	15,863

Chapter 5

Conclusion

This work has presented a thorough investigation and development of a single-ended LNA, alongside a detailed technical and economic comparison with a differential implementation for the CHARTS project. The study encompasses all phases, beginning with a brief review of the CHARTS project, followed by a theoretical analysis of key concepts and the practical realization of the amplifier, including its design, simulation, and implementation. It concludes with an overview of both differential and single-ended implementation scenarios, as well as the technical and economic comparison between them. This comprehensive approach ensures a deep understanding of the technical challenges and practical considerations involved in developing advanced LNA solutions for radio astronomy applications.

5.1 Overview of the Single-Ended LNA Design and Implementation

The starting point of the design process was the analysis of the CHARTS project, which highlighted the need for an LNA capable of operating in the 300–500 MHz frequency range. The design process involved selecting appropriate components, simulating the circuit using advanced software tools, and iteratively refining the design to meet the required specifications.

These results define the requirements for the LNA, which include a low noise temperature (approximately 50 K), high gain (in the range of 50–55 dB), and optimal input matching (50 Ω). The solution proposed in this work is a single-ended LNA comprising two stages of amplification, reaching a gain between 50–56 dB, a bias tee to power the amplifiers, and an input matching network that ensures reflections below −3 dB across the entire CHARTS band.

The implementation of the LNA consists of the design and fabrication of a PCB. It was designed using advanced CAD tools to ensure that the layout minimized parasitic effects and optimized performance. The components were soldered using an IC heater oven, and the final assembly was tested to verify that it met the design specifications.

The LNA was characterized using a VNA to measure the S-parameters, which confirmed that the amplifier met the required specifications for gain and reflections, as shown in fig. 3.1. However, the noise temperature was approximately 20 K higher than expected, as shown in fig. 3.5, while achieving reasonable input/output matching to 50 Ω (see figs. 3.2b and 3.2c). The results showed that the LNA achieved a noise temperature of 70 K and a gain exceeding 50 dB, with an input RL below −3 dB across the operating frequency range.

5.2 Technical-Economic Assessment of the implementations

The principal result coming from the technical-economic analysis is that both differential and single-ended implementations meet the project requirements, with the differential implementation achieving better performance (lower noise temperature), albeit at a slightly higher cost due to the need for a second-stage amplifier.

For the full CHARTS project, the differential implementation is the preferred choice due to recent developments in RFoF applied to ethernet cabling. This provides CHARTS with an enormous advantage, as the differential implementation enables signal transmission over long distances without significant loss or degradation. Additionally, it offers the opportunity to implement sensors for calibrating the array, making it ideal for the project's requirements.

The use of this novel technology enables a more efficient and cost-effective solution by eliminating the need for additional components and reducing the overall system complexity. This is particularly important for CHARTS, which aims to provide a high-performance radio telescope with minimal operational costs.

5.3 Future Work

This work successfully demonstrated the design, implementation, and evaluation of a single-ended LNA for the CHARTS project. The results indicate that the LNA meets the required specifications and is a viable solution for the project's needs. The technical-economic comparison with a differential implementation highlights the advantages of both approaches, with the differential implementation being more suitable for the project as it offers a more cost-effective solution at large scale, despite its implementation challenges.

It is important to mention that the single-ended LNA remains a valid solution for smaller-scale implementations, where time and complexity are more critical factors. The design and implementation process outlined in this work can serve as a reference for future projects requiring similar low-noise amplification solutions, such as the CHARTS-8 and CPT projects, already installed (see fig. 5.1), where the single-ended LNA provides a cost-effective and efficient option.

Future work will focus on testing scales of the complete array in Cerro Calán and Laguna

Figure 5.1: Photograph of the CPT project featuring a single-ended LNA installed at Cerro Calán, Chile. The LNA is mounted connected to the antenna at the feed using a custom 3D-printed support structure, ensuring optimal placement and stability. This implementation demonstrates the practical application of the single-ended LNA and serves as a precursor for the larger-scale CHARTS array.

Carén, starting with one antenna, differential and single-ended, then testing with CHARTS-8. Our team its aiming to implement 32 elements in site by January. We will assembly and test the differential setup, conduct measurments of RFI and the complete validation of the differential system. These represents a big step in the development of the CHARTS project, as it will allow for the evaluation of the performance of the LNA and provide insights into its operation and potential improvements.

Other areas of future research include the implementation of ethernet connections for the differential LNA, which would enable the use of RFoF technology to transmit signals over long distances without significant loss or degradation. This would further enhance the performance of the CHARTS project and provide a more efficient solution for large-scale implementations.

Acronyms

ADC analog-to-digital converter.

BURSTT Bustling Universe Radio Survey Telescope in Taiwan.

CHARTS Canadian-Chilean Array for Radio Transient Studies.
CHIME Canadian Hydrogen Intensity Mapping Experiment.
CPT CHARTS Path Finder Telescope.
CPU central processing unit.
CPW coplanar waveguides.

DAC digital-to-analog converter.
DAS Universidad de Chile's Astronomy Department.
DC direct current.
DM dispersion measure.
DUT Device Under Test.

ENR excess noise ratio.

F noise factor.
FDM frequency division multiplexer.
FPGA field programmable gate array.
FRB fast radio burst.

GPU graphics procesing unit.
GRex Galactic Radio Explorer.

IC integrated circuit.
ICH Infrared Circuit Heater.
IGM intergalactic medium.
ISM interstellar medium.

LNA low-noise amplifier.
LSB less significant bit.

MWL Millimeter Wave Lab Laboratory.

NF noise figure.
NIC network interface card.

PCB printed circuit board.

RAM random access memory.
RF radio frequency.
RFI radio frequency interference.
RFoF Radio Frequency over Fiber.
RFSoC radio frequency system-on-chip.
RL return loss ratio.
rms root mean square.

SFP Small Form-factor Pluggable.
SMA SubMiniature version A.
SMT surface mounted technology.
SNR signal-to-noise ratio.
SWR standing wave ratio.

UFRO Universidad de la Frontera.
UofT University of Toronto.

VLBI Very Long Baseline Interferometry.
VNA vector network analyzer.

Bibliography

Amazon. 2024, J-Tech Digital CAT6 Ethernet Cable - 150 ft High Speed Network Cable - Product Pricing and Availability, Seattle, WA, USA: Amazon. https://www.amazon.com/-/es/J-Tech-Digital-JTECH-CAT6-150-pies-transmisi%C3%B3n/dp/B01IPYVT3Y?th=1

Bethapudi, S., Spitler, L. G., Main, R. A., Li, D. Z., & Wharton, R. S. 2023, Monthly Notices of the Royal Astronomical Society, 524, 3303, doi: 10.1093/mnras/stad2009

Bhardwaj, M., Michilli, D., Kirichenko, A. Y., et al. 2024, The Astrophysical Journal Letters, 971, L51, doi: 10.3847/2041-8213/ad64d1

Braga, C. A., Cruces, M., Cassanelli, T., et al. 2025, Astronomy amp; Astrophysics, 693, A40, doi: 10.1051/0004-6361/202451905

Cassanelli, T., Leung, C., Rahman, M., et al. 2022, The Astronomical Journal, 163, 65, doi: 10.3847/1538-3881/ac3d2f

Cassanelli, T., Leung, C., Sanghavi, P., et al. 2024, Nature Astronomy, 8, 1429–1442, doi: 10.1038/s41550-024-02357-x

Cassanelli, T., Mena-Parra, J., Manosalva, S., et al. 2025, in 2025 19th European Conference on Antennas and Propagation (EuCAP), 1–5, doi: 10.23919/EuCAP63536.2025.10999353

CHIME/FRB Collaboration, Amiri, M., Andersen, B. C., et al. 2021, ApJS, 257, 59, doi: 10.3847/1538-4365/ac33ab

Connor, L., et al. 2021, Publications of the Astronomical Society of the Pacific, 133, 075001, doi: 10.1088/1538-3873/ac0bcc

Cruces, M., Spitler, L. G., Scholz, P., et al. 2021, MNRAS, 500, 448, doi: 10.1093/mnras/staa3223

Electronics, M. 2024, Amphenol Times Microwave Systems LMR-400-FR RF Coaxial Cable - Product Pricing and Availability, Mansfield, TX, USA: Mouser Electronics. https://www.mouser.com/ProductDetail/Amphenol-Times-Microwave-Systems/LMR-400-FR?qs=%252BRAvXJslkuACYqs9nmHLfQ%3D%3D

Gajjar, V., Siemion, A. P. V., Price, D. C., et al. 2018, ApJ, 863, 2, doi: 10.3847/1538-4357/aad005

Josaitis, A. T., Ewall-Wice, A., Fagnoni, N., & de Lera Acedo, E. 2022, Monthly Notices of the Royal Astronomical Society, 514, 1804, doi: 10.1093/mnras/stac916

Kester, W. 2014, ADC Noise Figure—An Often Misunderstood and Misinterpreted Specification, Tutorial MT-006, Analog Devices, Inc.

Lau, A. W. K., Vanderlinde, K., Mena-Parra, J., & Lansdale, C. 2024, in Ground-based and Airborne Instrumentation for Astronomy X, ed. J. J. Bryant, K. Motohara, & J. R. D. Vernet, Vol. 13096, International Society for Optics and Photonics (SPIE), 130969X, doi: 10.1117/12.3019137

Lee, T. H. 2004, Planar Microwave Engineering, doi: 10.1017/cbo9780511812941

Leung, C., Andrew, S., Masui, K. W., et al. 2024, arXiv e-prints, arXiv:2403.05631, doi: 10.48550/arXiv.2403.05631

Lin, H.-H., et al. 2022, Publications of the Astronomical Society of the Pacific, 134, 094106, doi: 10.1088/1538-3873/ac8f71

Lorimer, D. R., Bailes, M., McLaughlin, M. A., Narkevic, D. J., & Crawford, F. 2007, Science, 318, 777–780, doi: 10.1126/science.1147532

Macquart, J.-P., Prochaska, J., McQuinn, M., et al. 2020, Nature, 581, 391, doi: 10.1038/s41586-020-2300-2

Marcote, B., Nimmo, K., Hessels, J. W. T., et al. 2020, Nature, 577, 190, doi: 10.1038/s41586-019-1866-z

Mckinven, R., Gaensler, B. M., Michilli, D., et al. 2023, The Astrophysical Journal, 951, 82, doi: 10.3847/1538-4357/acd188

Mini-Circuits. 2022, PHA-13LN+ 50 Ohm 1 MHz to 1 GHz Monolithic Amplifier: Ultra High Dynamic Range, Datasheet Rev. A, Mini-Circuits. www.minicircuits.com

Mini-Circuits. 2023a, Monolithic Amplifier: PMA2-33LN+ Ultra Low Noise, High IP3 Datasheet, Brooklyn, NY, USA: Mini-Circuits. https://www.minicircuits.com/WebStore/dashboard.html?model=PMA2-33LN%2B

—. 2023b, Monolithic Amplifier: PMA2-63LN+ Wideband, Low Noise, Low Current Datasheet, Brooklyn, NY, USA: Mini-Circuits. https://www.minicircuits.com/pdfs/PMA2-63LN+.pdf

—. 2023c, SMT MMIC, Low Noise, Medium Power, Linear, pHEMT, Shutdown Amplifier: TSS-13LN+ Datasheet, Brooklyn, NY, USA: Mini-Circuits. https://www.minicircuits.com/WebStore/dashboard.html?model=TSS-13LN%2B

Nimmo, K., Hewitt, D. M., Hessels, J. W. T., et al. 2022, The Astrophysical Journal Letters, 927, L3, doi: 10.3847/2041-8213/ac540f

Petroff, E., Hessels, J. W. T., & Lorimer, D. R. 2022, The Astronomy and Astrophysics Review, 30, doi: 10.1007/s00159-022-00139-w

Pleunis, Z., Michilli, D., Bassa, C. G., et al. 2021, The Astrophysical Journal Letters, 911, L3, doi: 10.3847/2041-8213/abec72

Pozar, D. M. 2011, Microwave engineering (John Wiley & Sons)

Qorvo Inc. 2023, QPL9547 0.1 6 GHz Ultra Low-Noise Amplifier Datasheet, Datasheet Rev. D, Qorvo. www.qorvo.com

RealDigital. 2024, RFSoC 4x2 Reference Manual. https://www.realdigital.org

Shannon, R. M., Bannister, K. W., Bera, A., et al. 2025, Publications of the Astronomical Society of Australia, 1–36, doi: 10.1017/pasa.2025.8

Shila, K. A., Niedbalski, S., Connor, L., et al. 2025, Publications of the Astronomical Society of the Pacific, 137, 075001, doi: 10.1088/1538-3873/ade401

Stutzman, W. L., & Thiele, G. A. 2012, Antenna Theory and design (John Wiley & Sons)

Systems, T. M. 2023, LMR-400 Low Loss Communications Coax Datasheet, Connecticut, USA: Times Microwave Systems. https://www.mouser.com/datasheet/2/18/2/lmr_400_datasheet_1-3568900.pdf

Weinreb, S., & Shi, J. 2021, IEEE Transactions on Microwave Theory and Techniques, 69, 2345, doi: 10.1109/tmtt.2021.3061459

Zhang, B. 2023, Reviews of Modern Physics, 95, doi: 10.1103/revmodphys.95.035005

Annexes

Annex A: LPKF Procedure for PCB Manufacturing

This guide aims to teach the basic steps for using the LPKF machine. The laboratory has two LPKF machines: a mechanical one, which is used to cut contours, make fiducials, tracks, and vias if they are present in the design; and the LPKF laser, which is mainly used to print tracks and cutouts according to the design. Below are the standard steps for printing a PCB, using the design in Figure A.1 as a reference.

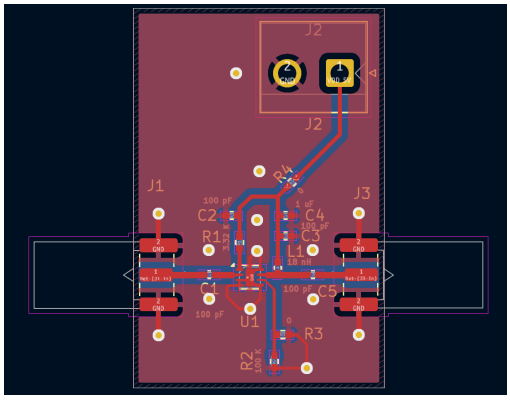

Figure A.1: Example of PCB design used as a reference for the LPKF procedure.

A.1 Generate .PL and .PM Files

Both the laser and mechanical machines use two programs: LPKF CircuitPro PL 2.0 and LPKF CircuitPro PM 2.0, respectively. The software has changed with each version; in version 2.0, the generation of fiducials and LMD files (files for use with the LPKF laser) is done in the PL program, while drills, contours, etc., are handled in the PM program. The following steps outline how to generate both files:

1. Copy the Gerber and drill files to a USB drive.
2. Turn on the computer near the mechanical LPKF, then the LPKF machine, and open the LPKF CircuitPro PL 2.0 program (IMPORTANT: this order must be followed).

3. Go to **Templates** → `LPKF ProtoLaser S` → *DoubleSided.cbf* (see Figure A.2).
4. Go to **Import** and select the corresponding Gerber and drill files.
5. Select the PCB layers as top layer, bottom layer, edge cuts, and DrillUnplated, as appropriate (the laboratory machines only have the Drilling Unplated option). See Figure A.3 for an example of how to assign the layers.
6. For fiducials, place them by clicking on the screen or entering coordinates; remember that it is preferable for them to be asymmetric.
7. Save as: save one file as `name_PM.cbf` and another as `name_PL.cbf`.
8. Continuing in the PL program, go to **Toolpath** → **Laser insulate** (option 4 recommended) → **Start**.

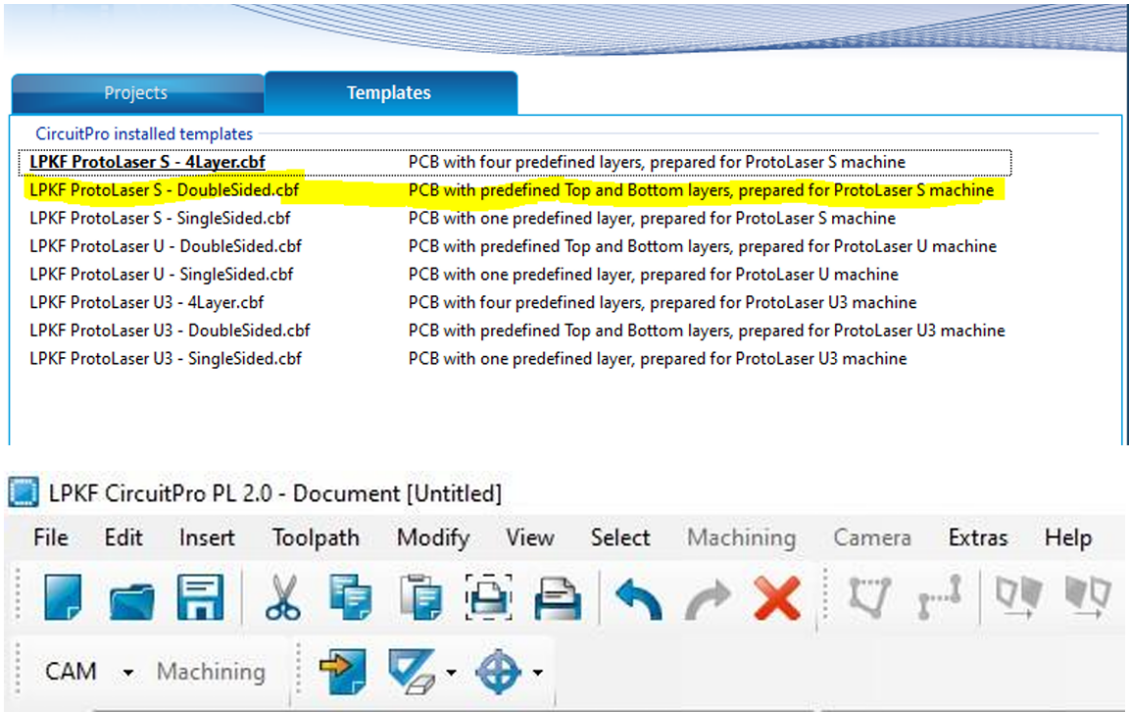

Figure A.2: Selecting the double-sided template in LPKF CircuitPro PL 2.0.

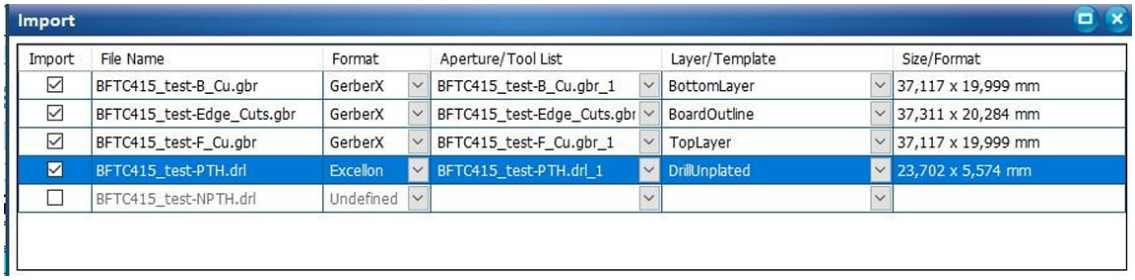

Figure A.3: Assigning PCB layers during the import process.

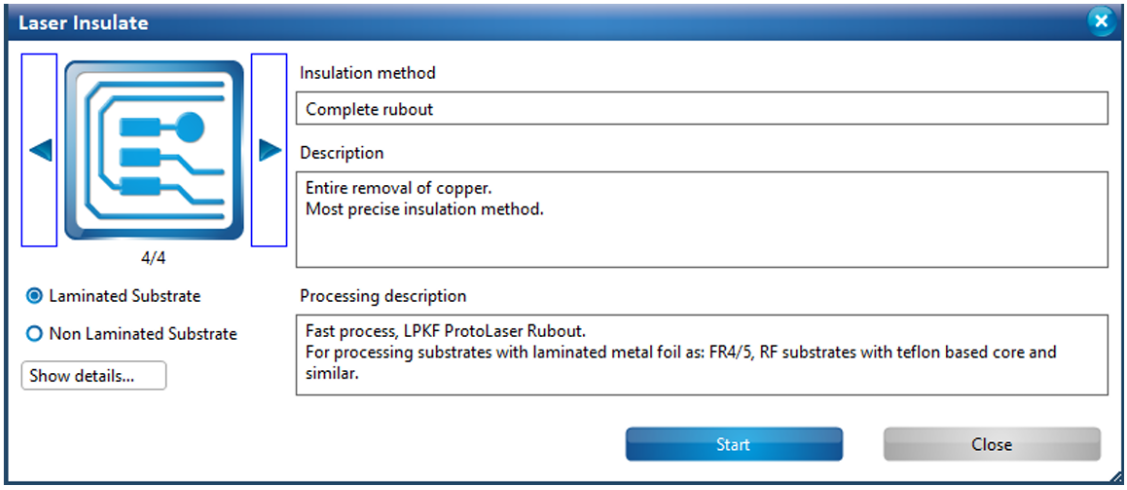

Figure A.4: Selecting the insulation method for laser processing.

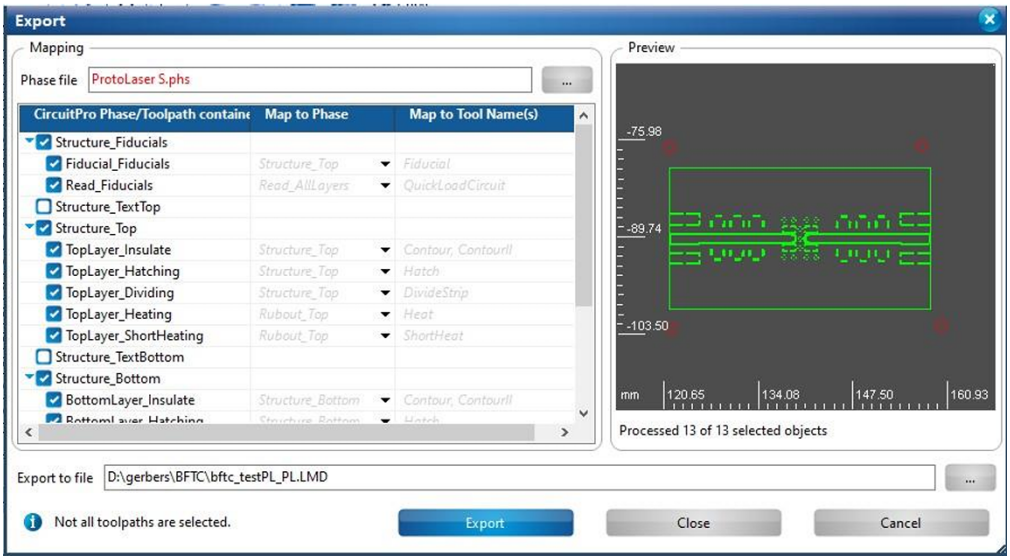

Figure A.5: Export screen for saving the .PL and .PM files.

A.2 Fiducials Generation at Mechanical LPKF

1. Open the Circuit Pro PM 2.7 program.
2. Open the file saved as `name_PM.cbf`.
3. Go to **Edit** → **Material settings** and ensure the parameters match your substrate.
4. Generate isolation and contour routing:
   (a) In **Isolation**, uncheck the isolation option.
   (b) In **Contour routing**, option 3 is recommended.
   (c) In **Drills**, select **assign to phase** → **Drilling unplated**.
   (d) In **Fiducials**, assign to phase → **Structure Fiducials**.

(e) Click **Start**.

5. Select position **P** to add the FR4 board to the mechanical LPKF. Remember to secure the board with tape.
6. Select **head** → the second option; this makes it easier to locate where the drill is pointing.
7. Choose the physical location where you want to place the PCB.
8. To move the camera to the chosen location, use the X/Y positioning arrows or the mouse cursor.
9. Move the board in the program to the selected area: first, deselect the **Mouse cursor** option, then go to **machining** → **placement** and move with the mouse.
10. Go to **Operate** → check **structure fiducials** → **play**.
11. Insert the corresponding drill bit (2mm recommended) and press OK. To adjust the drill bit, lower the lock and then turn it. The lock can only be lowered in one specific position; it is recommended to turn the lock only after pressing it down.
12. The machine will start heating up and proceed (remember that fiducials are made on the top layer).
13. Remove the drill bit (spiral drill 2mm).

Figure A.6: Top layer view in Circuit Pro PM 2.7.

A.3 Laser PCB Printing

Once the fiducials have been generated, the laser machine can accurately locate where the PCB will be printed. The following steps describe how to use the LPKF laser for PCB fabrication:

1. Turn on the LPKF laser PC, then the LPKF laser machine, and finally open the software.
2. Insert the USB drive containing the LMD file.
3. If the USB is not recognized, disconnect it from the PC and reconnect it before restarting the software.

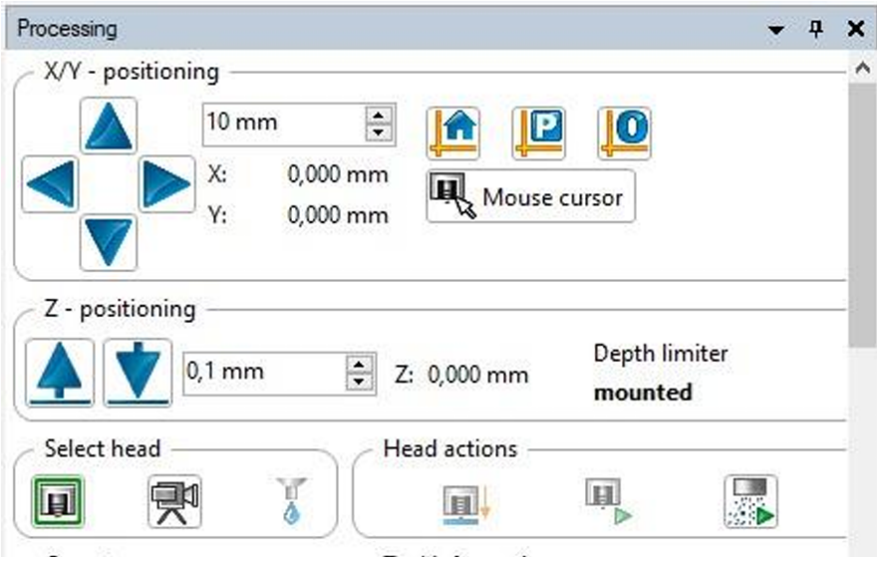

Figure A.7: Position controls for moving the camera and PCB in the LPKF software.

4. Before importing your file, it is recommended to first import a test file (e.g., `test_de_quemado` → `resonatorv3`) and place it at the edge of the board. Once finished, close and reopen the program.
5. Go to **File** → **Import** → `LMD-LPR`.
6. Select the routine, which defines the laser tool and its power. (Recommended routine for FR4 as of this document: `LPKF_FR4_35um_1Oz_Cu_v5.3FL`)
7. To insert the PCB into the LPKF, move the base using the icon between **Start** and **LMD+**.
8. Go to **Job** → **Material size** and enter the correct board dimensions.
9. Select the flashlight icon and move the laser to one of the fiducials.
10. Move the PCB design in the software to align with the fiducial mark (button to the right of Y).
11. Select that you are working on the top layer:
    (a) Go to **Edit** → **Phases**.
    (b) Deselect the soldering side (if possible; sometimes it cannot be removed).
12. Click **ALL+** → **Start**; the machine will search for the fiducials (if not properly aligned, adjust them manually).
13. Wait for the laser to warm up; the expected power is around 14 W (this usually takes about 9 minutes).
14. For the bottom layer, go to **Edit** → **Phases** and deselect the enable option for the top layer (ensure the fiducials are in the correct order). If the enable option cannot be edited, start a new project.
15. If the fiducials are not correctly aligned, restart the software; if the problem persists, restart the PC.

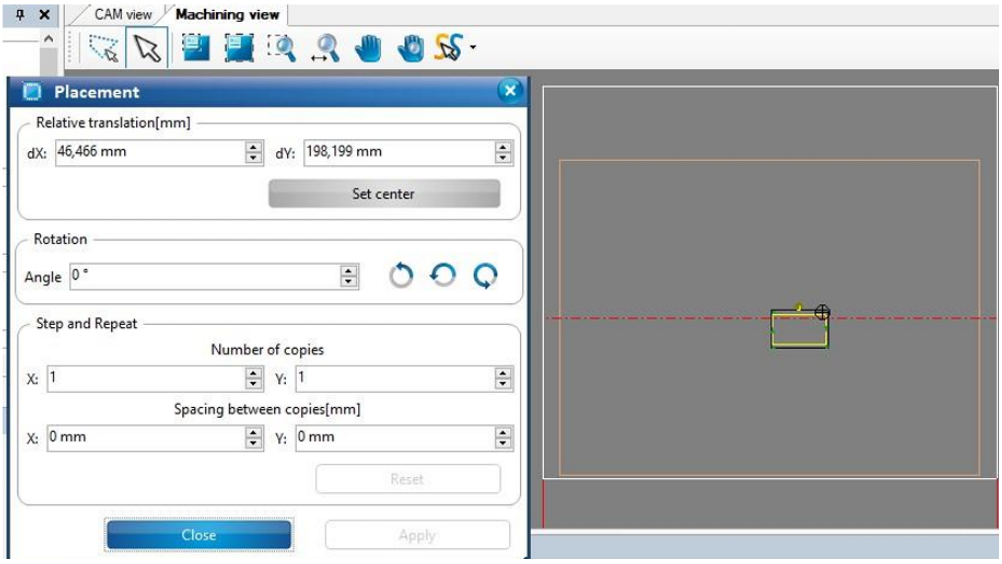

Figure A.8: Placing the PCB in the desired position within the software.

A.4 Back to Mechanical LPKF for Contour Cutting

The only remaining steps are to drill the holes and cut the PCB outline. The machine is programmed to perform the drills on the bottom layer and the contour cut on the top layer.

1. Move the PCB back to the mechanical LPKF and open the PM program (the `name_PM` file should still be open).
   (a) Insert the board with the bottom layer facing up.
   (b) Go to **Operate** → **drilling unplated** → **start** (the machine will begin to adjust the focus). See fig. A.9.
   (c) The machine may not find the fiducials since the board was moved; after it fails to locate them, manually adjust the position using the X/Y positioning arrows. Accept the current position (see fig. A.11).
2. The software will prompt you to change the drill bit; follow the tool changes as instructed by the program.
3. To cut the contour, go to **Operate** → **contour routing** and the machine will proceed with the same process.
4. Clean the PCB.

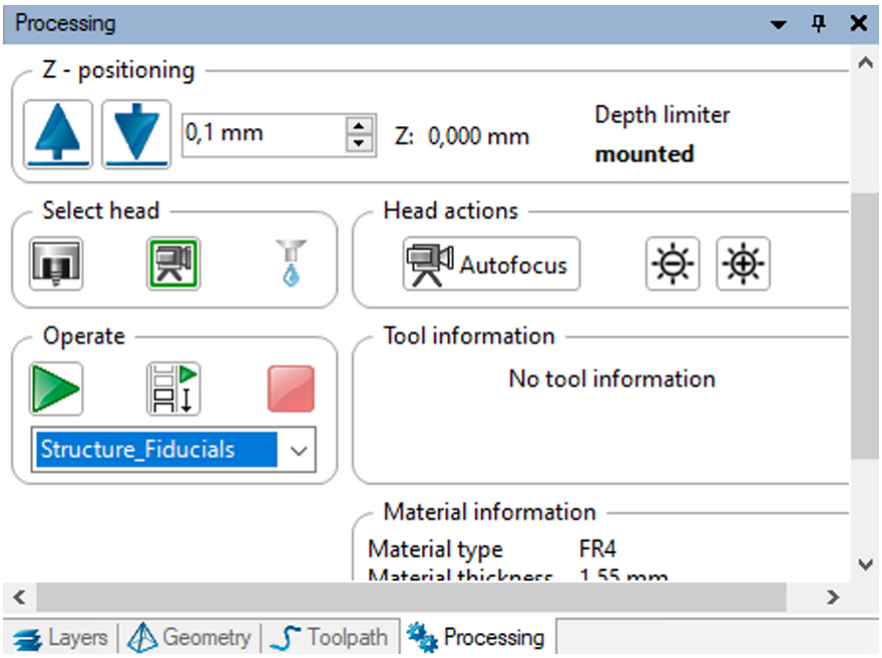

Figure A.9: Selecting the **Operate** menu and structure fiducials option.

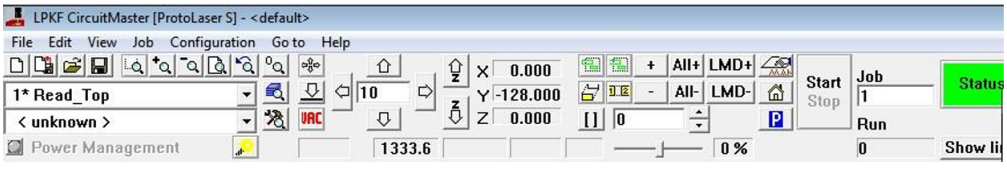

Figure A.10: Top bar of the LPKF laser software interface.

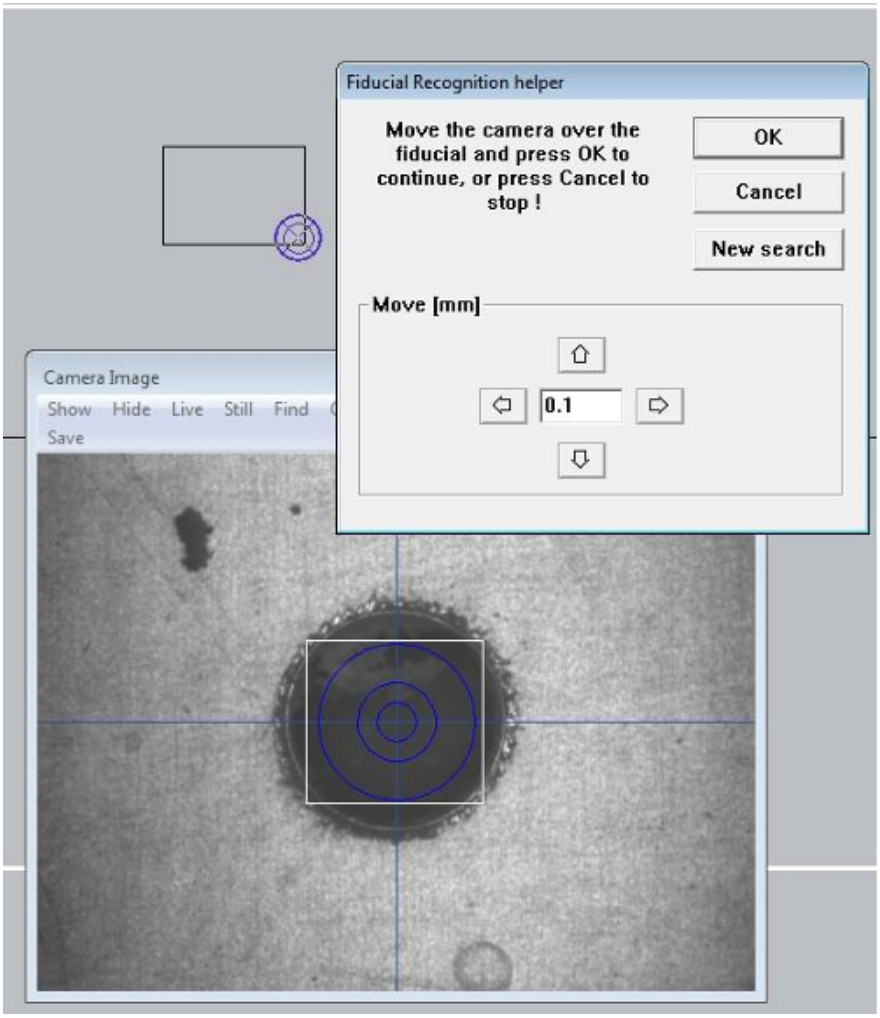

Figure A.11: Fiducial recognition process in the LPKF laser software.